LEVEL II

12 SC

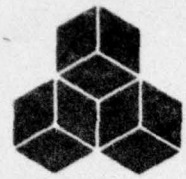

SYSTEMS, SCIENCE AND SOFTWARE

SSS-R-78-3627

ANALYSIS OF TWO DECOUPLED EXPLOSION SIMULATIONS

T. C. BACHE
J. F. MASSO

TOPICAL REPORT

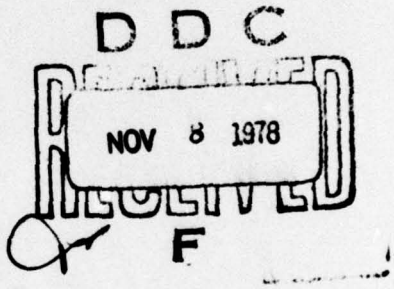

SPONSORED BY
ADVANCED RESEARCH PROJECTS AGENCY
ARPA ORDER NO. 2551

This research was supported by the Advanced Research Projects Agency of the Department of Defense and was monitored by AFTAC/VSC, Patrick Air Force Base, Florida, 32925, under Contract No. F08606-76-C-0041.

APRIL 1978

P. O. BOX 1620, LA JOLLA, CALIFORNIA 92038, TELEPHONE (714) 453-0060

AFTAC Project Authorization No. VELA/T/7712/B/ETR

ARPA Order 2551, Program Code 8F10

Effective Date of Contract: October 1, 1976

Contract Expiration Date: September 30, 1978

Amount of Contract: $435,087

Contract No. F08606-76-C-0041

Principal Investigator and Phone No.

Dr. Thomas C. Bache, (714) 453-0060, Ext. 337

Project Scientist and Phone No.

Captain Michael J. Shore, (202) 325-7581

VT/7712/B/ETR

UNCLASSIFIED

SECURITY CLASSIFICATION OF THIS PAGE (When Data Entered)

REPORT DOCUMENTATION PAGE

READ INSTRUCTIONS BEFORE COMPLETING FORM

1. REPORT NUMBER

2. GOVT ACCESSION NO.

3. RECIPIENT'S CATALOG NUMBER

4. TITLE (and Subtitle)

ANALYSIS OF TWO DECOUPLED EXPLOSION SIMULATIONS,

5. TYPE OF REPORT & PERIOD COVERED

Topical Report,

6. PERFORMING ORG. REPORT NUMBER

SSS-R-78-3627

7. AUTHOR(s)

Thomas C. Bache
J. F. Masso

8. CONTRACT OR GRANT NUMBER(s)

F08606-76-C-0041

9. PERFORMING ORGANIZATION NAME AND ADDRESS

Systems, Science and Software
P. O. Box 1620
La Jolla, California 92038

10. PROGRAM ELEMENT, PROJECT, TASK AREA & WORK UNIT NUMBERS

Program Code No. 6F10
ARPA Order No. 2551

11. CONTROLLING OFFICE NAME AND ADDRESS

VELA Seismological Center
312 Montgomery Street
Alexandria, Virginia 22314

12. REPORT DATE

April 1978

13. NUMBER OF PAGES

42

14. MONITORING AGENCY NAME & ADDRESS (if different from Controlling Office)

51 p.

15. SECURITY CLASS. (of this report)

Unclassified

15a. DECLASSIFICATION DOWNGRADING SCHEDULE

16. DISTRIBUTION STATEMENT (of this Report)

Approved for Public Release; Distribution Unlimited.

17. DISTRIBUTION STATEMENT (of the abstract entered in Block 20, if different from Report)

18. SUPPLEMENTARY NOTES

19. KEY WORDS (Continue on reverse side if necessary and identify by block number)

Nuclear Explosion Seismology
Explosion Source Theory
Explosion Decoupling
Theoretical Seismogram Generation

78 11 06 099

20. ABSTRACT (Continue on reverse side if necessary and identify by block number)

Two axisymmetric ground motion calculations were carried out by Applied Theory, Incorporated to simulate 25 kt decoupled nuclear explosions in mined cavities in salt. One cavity was spherical with a radius of 66 meters while the other was a 3/1 aspect ratio ellipsoid of revolution. Both had the same volume. Results of the two calculations were analyzed to determine the character of the teleseismic body and surface waves. → (cont'd)

DD FORM 1 JAN 73 1473 EDITION OF 1 NOV 65 IS OBSOLETE

388507

UNCLASSIFIED

SECURITY CLASSIFICATION OF THIS PAGE (When Data Entered)

20. ABSTRACT (continued)

The spherically symmetric portion of the field is slightly (20 to 25 percent) smaller for the spherical cavity. Comparing to results of tamped explosions, the decoupling factor for this case is about 140 at one Hertz. The radiation from the ellipsoidal cavity is substantially perturbed from spherical symmetry; the maximum S wave amplitudes are nearly three times as large as maximum P wave amplitudes at 1.0 Hz. However, theoretical body and surface wave seismograms indicate that the m_b and M_s values are not substantially different for the two cavities.

TABLE OF CONTENTS

LIST OF ILLUSTRATIONS

LIST OF ILLUSTRATIONS (continued)

1. INTRODUCTION

Two axisymmetric ground motion calculations were carried out by Applied Theory, Incorporated (ATI) to simulate decoupled explosions in mined cavities in salt. Results from these calculations were provided to Systems, Science and Software (S^3) for analysis to determine the character of the teleseismic signatures of these decoupled explosions.

The ATI calculations were in a homogenous whole space and were carried into the elastic regime where the divergence and curl of the displacement field were monitored. From these quantities an equivalent elastic source representation was computed for each of the two calculations. In the first case the mined cavity was spherical and the equivalent elastic source is a center of dilatation. In the second calculation the cavity was an ellipsoid of revolution. In this case, the equivalent elastic source includes higher order terms representing the departure from spherical symmetry.

In Section 2 we briefly describe the material properties and geometry for the two source calculations. In Section 3, the method for determining the equivalent elastic source is described. It is based on an expansion of the displacement field in spherical harmonics. The source is then described by a series of multipole coefficients. An advantage of this representation is that the near- and far-field terms and the P and S waves are conveniently separated. Also, the long-period asymptotic behavior of the coefficients can be bounded.

In Sections 4 and 5, we describe the multipole coefficients in the time and frequency domains. While the time domain coefficients are exact, apart from numerical error, there is some ambiguity in the Fourier transformed coefficients at long periods. This arises from the fact that the calculations are carried out for only a few tenths of a second while our primary interest is in the character of the solution

at periods of 1 to 30 seconds. The ambiguity results from the fact that we cannot be sure the values at the last computed time step are close to the true static solution. This is particularly a problem for the S wave portion of the solution. The best we can do is to attempt to bound the contribution of the long period S waves.

As far as the spherically symmetric portion of the field is concerned, we find that the spherical cavity is slightly more decoupled (20 to 25 percent) than the elliptical cavity. The higher order terms increase the radiation from the latter, increasing the decoupling difference between the two. Comparing other estimates for the source function for a tamped explosion in salt we find decoupling factors ranging from 300 at long period to less than 100 at frequencies greater than 3 Hertz.

Using the equivalent elastic source representation, body and surface waves synthetic seismograms were computed for the two sources. Results are presented in Sections 6 and 7. While changing interference between the direct P, pP and sP phases can lead to minor variations in m_b and the waveforms, we conclude that radiation pattern affects are unimportant for short period body waves and m_b. That is, the m_b for the ellipsoidal cavity is not substantially different than that for the spherically symmetric cavity. For surface waves the results are very much the same. It is true that the ellipsoidal cavity will generate Love waves. However, the Rayleigh wave radiation patterns do not differ substantially from the spherically symmetric case. These conclusions are based on a series of calculations assuming the largest reasonable contribution from the S wave portion of the field and rotating the source to orientations expected to give optimum radiation pattern effects.

In Section 8 we compare the results obtained here to results from somewhat similar calculations done several years ago at S^3 and reported by Cherry, Bache and Patch (1975).

These calculations were for tamped explosions in cylindrical cavities and lead to sources with radiation patterns similar to those from the ellipsoidal cavity. For these earlier calculations the results were that the m_b and M_s were not substantially different than for the same sized explosion in a spherical cavity.

2. SOURCE CALCULATIONS

Two axisymmetric ground motion calculations were carried out by ATI to simulate explosions in mined cavities in salt. One cavity was spherical and the other was an ellipsoid of revolution or prolate spheriod. Pertinent information provided to S^3 about these calculations is summarized in this section. The two cavities were assumed to be mined from a medium in a uniform hydrostatic stress of 181 bars. The calculations were initiated with an initial stress field that included the effect of mining the cavities. The spherical cavity has a radius of 66 meters while the prolate spheriod has a 3/1 aspect ratio. The volume of the two is the same. The pertinent dimensions and material properties are listed in Table 1.

The calculations were carried into the elastic regime and the divergence and curl of the displacement field were monitored at a constant radius of 928 meters. These data, the time histories of the divergence and curl at one degree intervals on the radius, were provided to S^3 for analysis. The remainder of this report is devoted to describing the results of that analysis.

3. EQUIVALENT ELASTIC SOURCE - THE METHOD

This problem is quite similar to those studied by Cherry, Bache and Patch (1975) who were interested in tamped explosions in cylindrical cavities. The methods applied are identical to those in the earlier work. The geometry is shown in Figure 1. We first compute multipole coefficients in the time domain from

$$A_{no}^{(4)}(\hat{R},t) = (2n+1)\int_0^{\pi/2} \chi_4(\hat{R},\theta,t)\, P_n^o(\cos\theta)\sin\theta\, d\theta, \tag{1}$$

$n = 0, 2, 4, \ldots,$ and

TABLE 1

PROPERTIES FOR ATI SOURCE CALCULATIONS IN SALT

Depth of Burial (m)	819
Density, ρ (gm/cm^3)	2.24
P Wave Velocity, α (km/sec)	4.4152
S Wave Velocity, β (km/sec)	2.5
Yield (KT)	25
Initial Cavity Volume (m^3)	1.2×10^6
Spherical Cavity Diameter (m)	132
Prolate Spheroid Major Axis (m)	275
Prolate Spheroid Minor Axis (m)	92

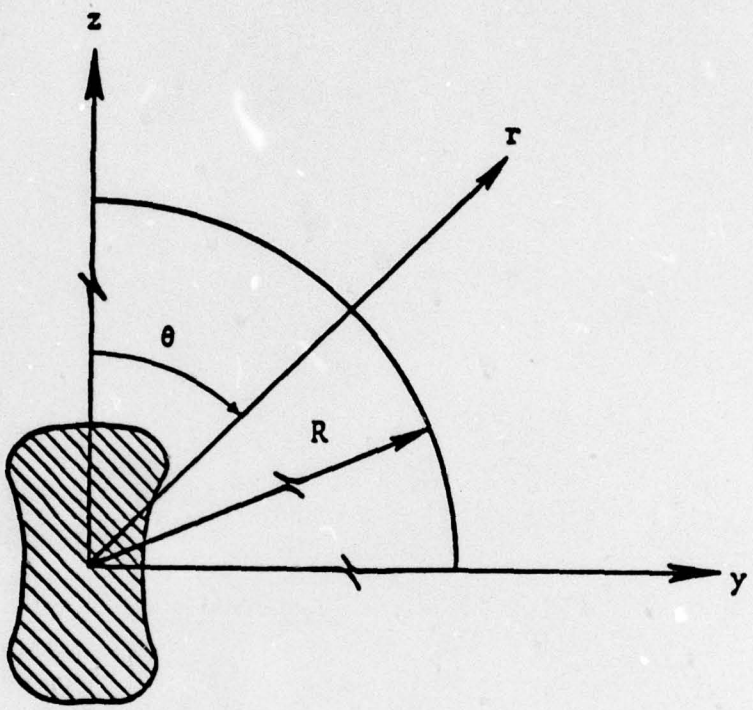

Figure 1. Geometry and coordinate system for a cavity section at fixed azimuth angle.

$$B_{n1}^{(1)}(\hat{R},t) = \frac{(2n+1)(n-1)!}{(n+1)!} \int_o^{\pi/2} \chi_r(\hat{R},\theta,t)\, P_n^1(\cos\theta) \sin\theta\, d\theta,$$

$$A_{n1}^{(2)}(\hat{R},t) = - B_{n1}^{(1)}(\hat{R},t), \quad n = 2, 4, 6, \ldots,$$

with

$$\chi_4 = \nabla \cdot \underset{\sim}{u} \ ,$$

$$\underset{\sim}{\chi} = \frac{1}{2} \nabla \times \underset{\sim}{u} \ , \tag{2}$$

$$\chi_r = \left(\chi_1^2 + \chi_2^2 \right)^{1/2} \ ,$$

where the curl and divergence are monitored on the spherical surface with radius $\hat{R}$. The axisymmetry is accounted for in deriving Equation (1).

The next step is to compute the frequency domain multipole coefficients from the following transformation:

$$\begin{pmatrix} A_{mn}^{(\alpha)}(\omega) \\ B_{mn}^{(\alpha)}(\omega) \end{pmatrix} = \frac{1}{h_n^{(2)}(k_\alpha R)} \int_{-\infty}^{\infty} \begin{Bmatrix} A_{nm}^{(\alpha)}(\hat{R},t) \\ B_{nm}^{(\alpha)}(\hat{R},t) \end{Bmatrix} e^{-i\omega t}\, dt, \tag{3}$$

$\alpha = 1, 2, 3, 4$, with $\alpha = 4$ indicating the dilatational or P wave coefficients. Having these coefficients, we can compute the whole space displacements from

$$\chi_\alpha(\underset{\sim}{R},\omega) = \sum_{n=o}^{\infty} h_n^{(2)}(k_\alpha R) \sum_{m=o}^{n} \left(A_{nm}^{(\alpha)}(\omega) \cos m\phi + B_{nm}^{(\alpha)}(\omega) \sin m\phi \right)$$

$$\cdot P_n^m(\cos\theta) \tag{4}$$

where the vector $\underset{\sim}{R}$ has components R, θ, ϕ in a spherical coordinate system. Then the Fourier transformed displacement is

$$\hat{\underset{\sim}{u}}(R,\omega) = -\frac{1}{k_\alpha^2}\,\nabla\hat{\chi}_4 + \frac{2}{k_\beta^2}\,\nabla \times \hat{\underset{\sim}{\chi}} \quad , \tag{5}$$

where k_α and k_β are the P and S wave numbers.

Using the multipole coefficients to represent the source, we can compute body and surface waves in layered earth models using methods outlined by Bache and Harkrider (1976) and Harkrider and Archambeau (1978). While the original coefficients are computed with the source oriented as shown in Figure 1, they can be rotated (Minster, 1976) to represent a source at an arbitrary orientation with respect to a fixed coordinate system.

The spherically symmetric calculation can also be represented by a reduced displacement potential defined by

$$u(R,t) = \frac{\partial}{\partial R}\left[\frac{\Psi(t-R/\alpha)}{R}\right] \quad . \tag{6}$$

In terms of the multipolar expansion we have

$$A_{oo}^{(4)}(\omega) = -\frac{\omega^2}{\alpha^3}\,\hat{\Psi}(\omega) \quad , \tag{7}$$

and all other multipoles vanish. Also,

$$\hat{\Psi}(\omega) = \frac{i\,\alpha^2\,R}{\omega}\,e^{ik_\alpha R}\,\hat{\chi}_4(R,\omega) \tag{8}$$

where $\hat{\chi}_4$ is simply the Fourier transform of the divergence. Another useful relationship is

$$\frac{\ddot{\Psi}(t-R/\alpha)}{R\alpha^2} = -\nabla \cdot \underset{\sim}{u}(R,t) \quad . \tag{9}$$

From these equations we can derive some limiting behavior for the multipole coefficients that can be used to check the solution. We know

$$\lim_{\omega \to 0} \hat{\Psi}(\omega) = \lim_{t \to \infty} \Psi(t) = C \tag{10}$$

where C is some constant. Then from Equations (9) and (10)

$$\lim_{T \to \infty} \int_0^T \nabla \cdot \underset{\sim}{u}(R,t)\, dt = 0 \quad . \tag{11}$$

From Equation (1) we see that

$$A_{oo}^{(4)}(R,t) = - \nabla \cdot \underset{\sim}{u}(R,t) \tag{12}$$

and the limiting relationship in Equation (11) applies to the time domain monopole as well.

For the higher order coefficients we have only the requirement that

$$\lim_{t \to \infty} \quad A_{nm}^{(\alpha)}(R,t) = C, \; n \geq 2 \quad , \tag{13}$$

and C may be a positive or negative constant or zero. If $C \neq 0$, then

$$\lim_{\omega \to 0} \quad A_{nm}^{(\alpha)}(\omega) \approx \omega^n \quad , \tag{14}$$

otherwise the falloff is at ω^{n+1} or steeper at low frequency.

4. MULTIPOLE COEFFICIENTS IN THE TIME DOMAIN

The first step is to apply Equation (1) and obtain the multipole coefficients in the time domain. The monopole and quadrupole (double-couple) terms for the spherical cavity calculation are shown in Figure 2. If the calculation were spherically symmetric, as it would be in the absence of numerical errors in the finite difference code, the quadrupole terms would vanish. Indeed, we see that the peak values are down by one or two orders of magnitude. Also, note from Equation (12) that the monopole is just the negative of the divergence of the displacement field for a spherically symmetric explosion. The higher order terms are nonzero because the $\nabla \cdot \underset{\sim}{u}$ is not exactly the same at all points monitored in the ATI calculations.

The time domain multipole coefficients for the ellipsoidal cavity are shown in Figure 3. The coefficients for $n \leq 4$, the monopole, quadrupole and octupole, are plotted. Comparing to the coefficients in the spherical cavity case, we see that the monopole is somewhat smaller but is otherwise not greatly different. However, the higher order terms are now the same order of magnitude as the leading term, the monopole. It is difficult to estimate the relative importance of these coefficients because of differences in frequency content. For this reason the radiation field will be studied in the frequency domain.

A prominent feature of the P wave coefficients is an oscillation at 30 Hz. This is apparently related to a natural frequency of the numerical grid (Neil Perl, ATI, personal communication).

5. MULTIPOLE COEFFICIENTS IN THE FREQUENCY DOMAIN

To obtain the frequency-domain multipole coefficients we apply the transformation in Equation (3). While the time domain coefficients of Figures 2 and 3 are exact, apart from numerical error, there is some ambiguity in the transformed coefficients at long periods. Examining the coefficients for the ellipsoidal cavity, Figure 3, the ambiguity results from the fact that we cannot be sure the values at the last time step are close to the static solution.

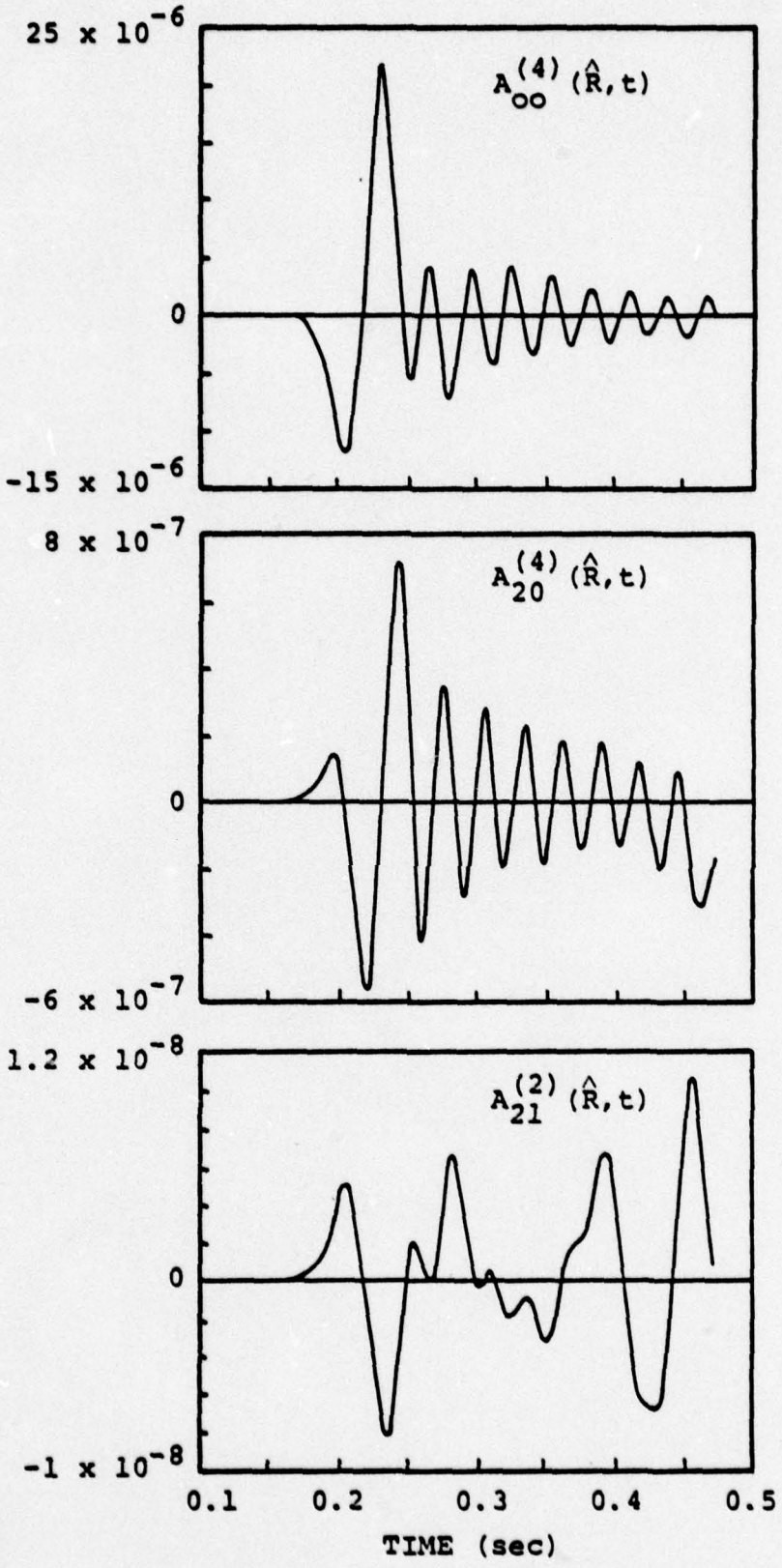

Figure 2. The monopole and quadrupole terms are plotted for the spherical cavity at the monitoring radius $\hat{R}$ = 928 meters.

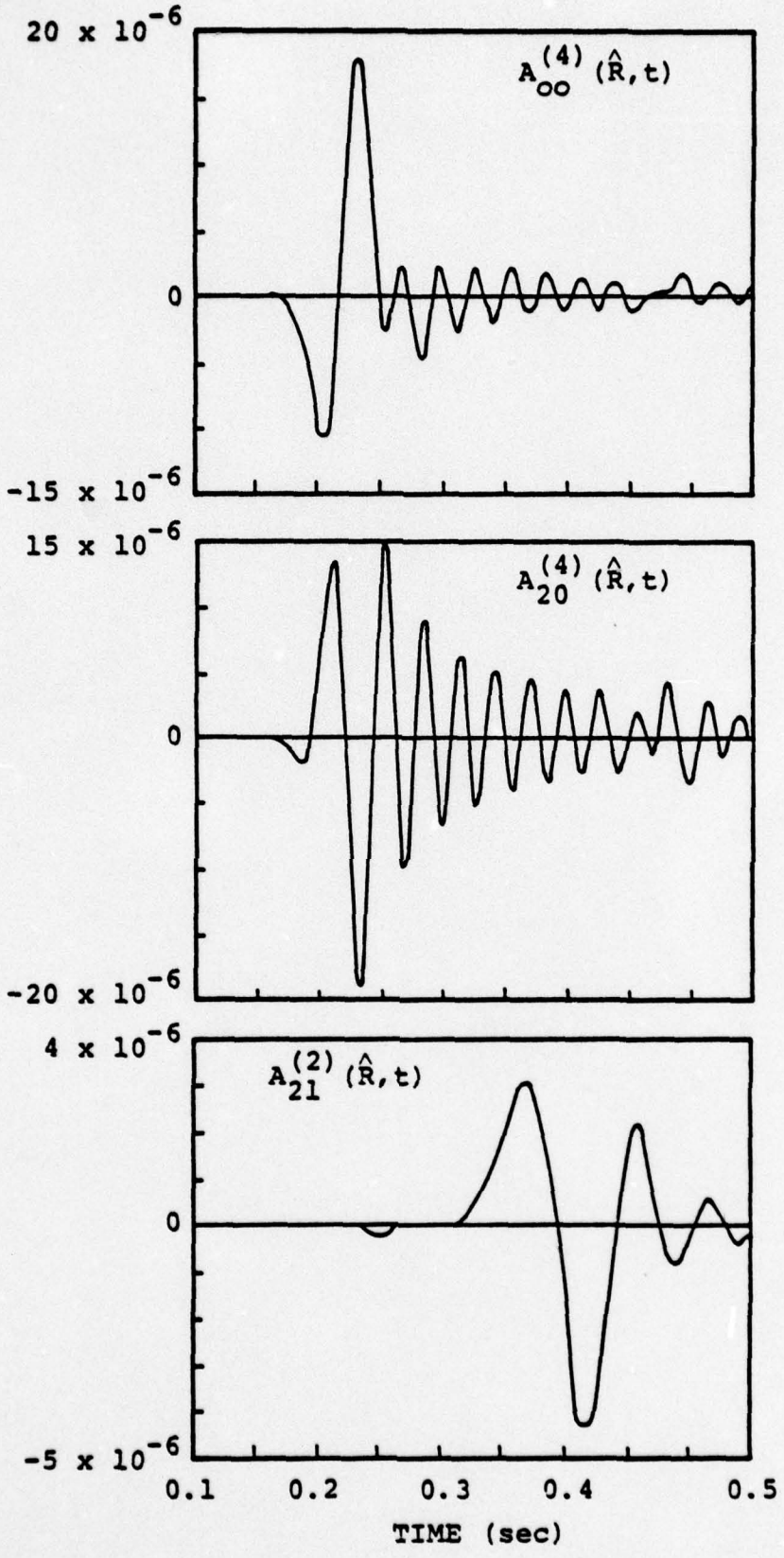

Figure 3. The monopole, quadrupole and octupole terms are plotted for the ellipsoidal cavity. The radius $\hat{R}$ = 928 meters.

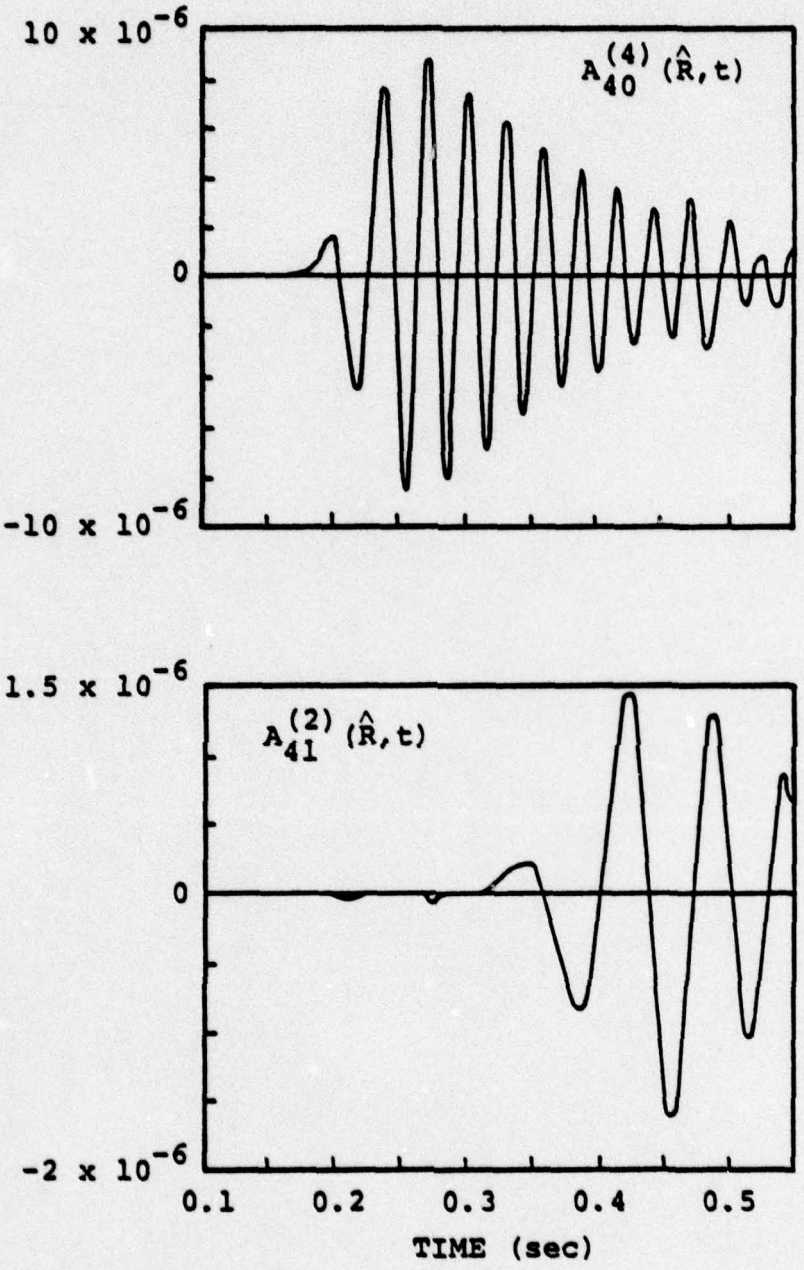

Figure 3. (continued)

The dilatational coefficients, $A_{no}^{(4)}$, have a signal lasting about 0.38 seconds. Therefore, estimates of these coefficients at frequencies less than 2.6 Hz will be limited by the accuracy of our estimate of the static solution. For the rotational coefficients the same is true for frequencies less that 4 Hz.

For obtaining $A_{oo}^{(4)}(\omega)$ we take advantage of the limiting relationships of Equations (11) and (12). The quantity

$$g(T) = \int_o^T A_{oo}^{(4)}(\hat{R},t)\, dt$$

is plotted in Figure 4 for the two source calculations. Since g(T) is nearly zero at long times, we can with confidence set g(T) = 0 for T greater than the computational time. Then our long period estimate of $A_{oo}^{(4)}(\omega)$ should be quite good.

For the quadrupole and higher order terms the long period values depend on our estimate of the static values. There are many ways this estimate could be made, but the simplest choices are these:

1. Set the coefficients to zero at times greater than the last time step.

2. Assume the value at the last time step is the static value.

As is clear from the plots in Figure 3, neither choice is correct, especially for the octupole terms. However, as was explained in connection with Equation (14), if we choose the first alternative, the coefficients $A_{nm}^{(\alpha)}$ will fall off as ω^{n+1} at low frequency. Otherwise, they will fall off as ω^n. Therefore, we will look at the results from both alternatives and attempt to bound the true solution.

The multipole coefficients for the ellipsoidal cavity are plotted in Figure 5 after dividing by ω^2. It can be shown

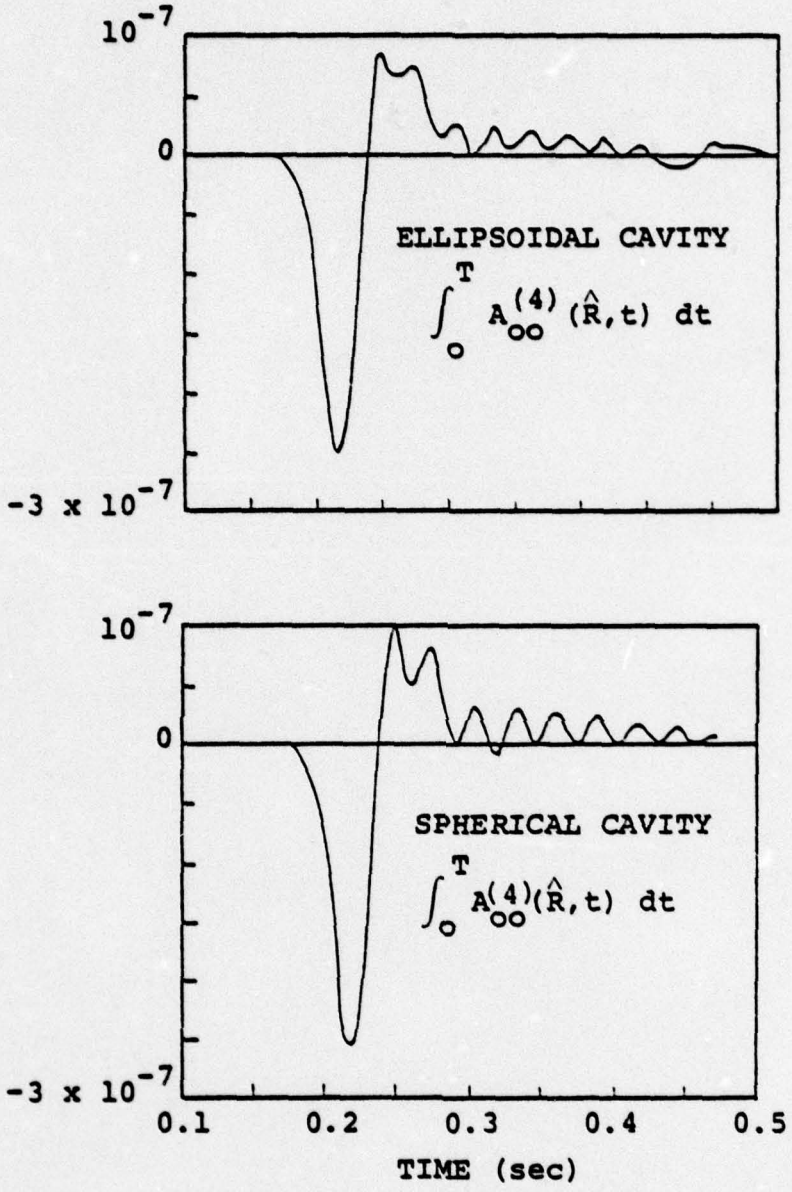

Figure 4. The time integral of the monopole is plotted for the two source calculations.

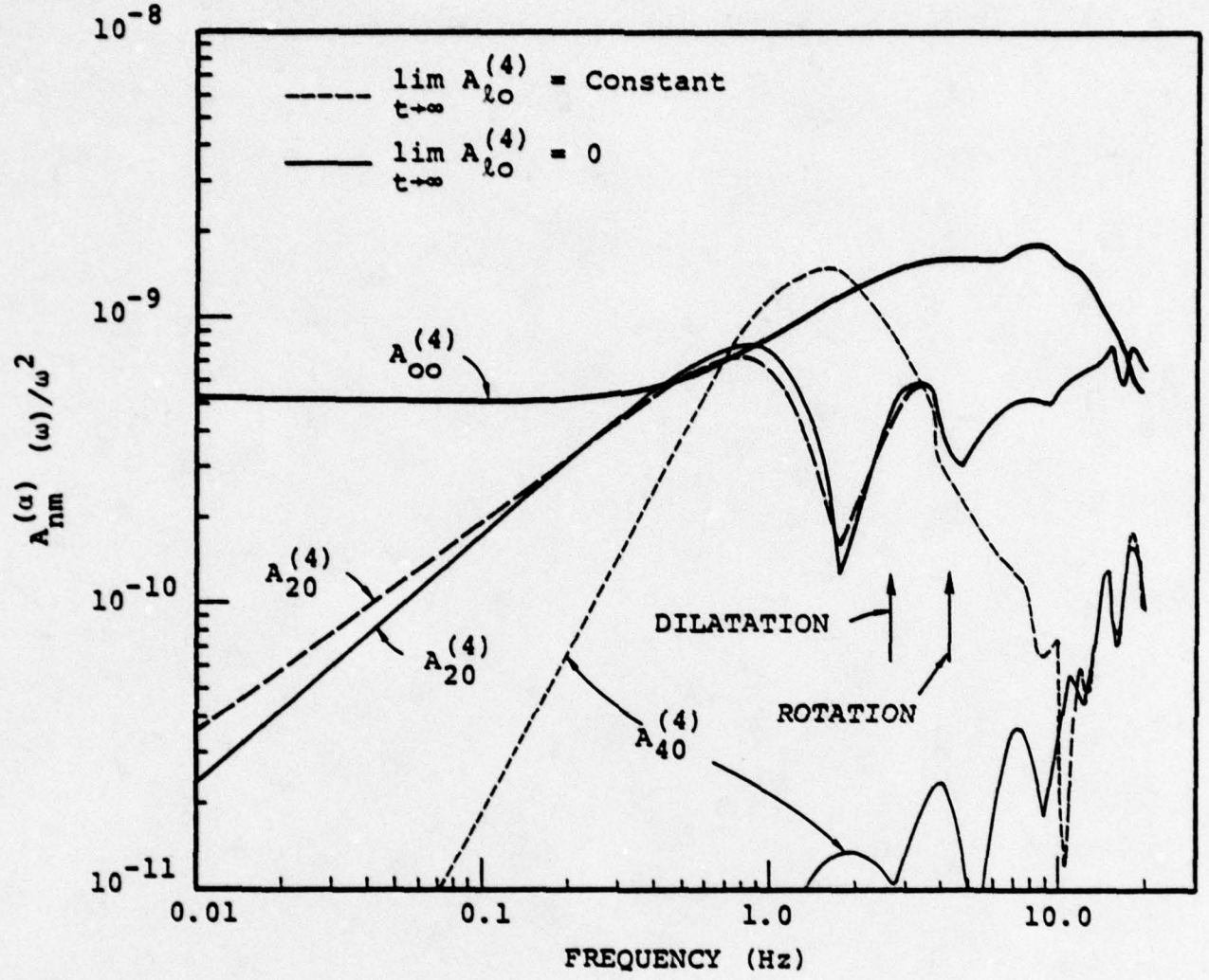

Figure 5a. The "P wave" multipole coefficients for the ellipsoidal cavity are plotted after normalization by ω^2. The arrows labeled "Dilatation" and "Rotation" indicate the lowest frequencies sampled by the finite difference calculation; that is, the inverse of the signal duration.

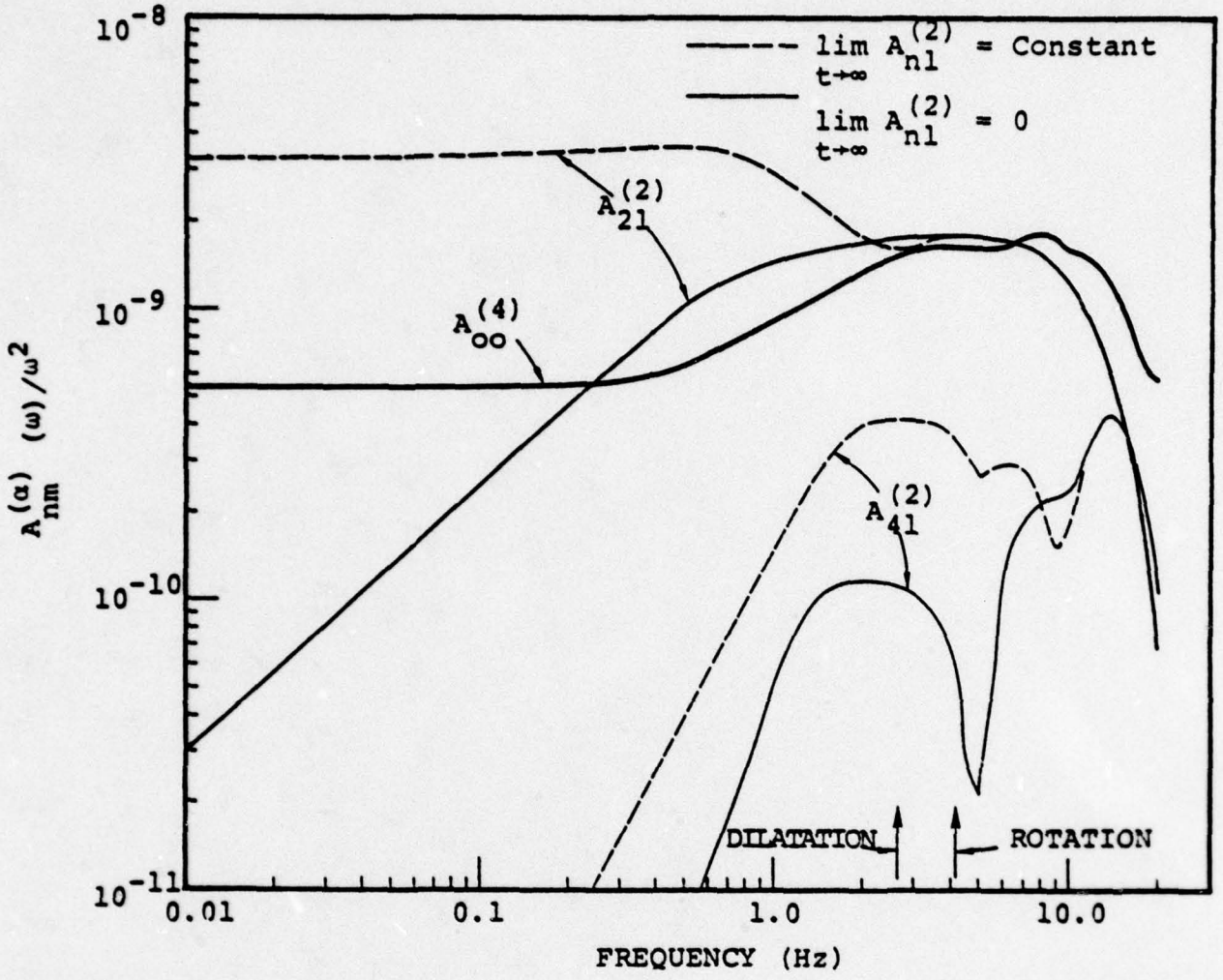

Figure 5b. The "S wave" coefficients are compared to the P wave monopole.

from Equations (4) and (5) that the far-field displacement is directly proportional to a sum of terms of the form $A_{nm}^{(\alpha)}/\omega^2$. Therefore, the curves in Figure 5 are proportional to the far-field displacement spectrum. From Figure 5a we draw the following conclusions for the dilatational or far-field P wave portion of the field ($A_{no}^{(4)}(\omega)$).

- The dilatational portion of the radiation field is nearly spherically symmetric for periods longer than 5 or 10 seconds.
- The quadrupole term is significant at frequencies near one Hertz, the important frequencies for teleseismic short period body waves.
- It does not matter very much whether we assume the late-time double-couple ($A_{20}^{(4)}$) is zero or equal to the value at the last computed time step. This indicates that the computation is essentially complete as far as this component is concerned.
- The octupole term is very small if it has a zero static limit. If the last time point were the static limit, the octupole term makes a large contribution near one Hertz. However, looking at Figure 3, this seems to be an unreasonable assumption.

For the rotational or far-field S wave portion of the radiation field, the story is somewhat different. We note the following:

- The octupole term, $A_{41}^{(2)}$, is not important.
- For the double-couple term our assumption about the long time behavior makes a huge difference

at long period. This indicates that the calculation has not been carried out long enough for the rotational part of the field to pass completely through the monitoring surface. This is also apparent from the plots in Figure 3.

- At the M_s period ($\approx$ 20 seconds) the S wave coefficient is either 0.25 or 6.5 times the P wave coefficient. The range is therefore a factor of 26. The truth probably lies somewhere between.

In Figure 6 we compare the monopole for the ellipsoidal cavity to that for the spherical cavity. The spherically symmetric contribution to the displacement field is smaller for the spherical cavity below 10 Hertz. This result seems a bit surprising because the source yield and cavity volume are the same for both calculations and the field for the ellipsoidal cavity is augmented by contributions from higher order terms.

Radiation patterns showing the excitation of far-field P and S waves at selected frequencies are shown in Figure 7 for the spherical cavity and Figure 8 for the ellipsoidal cavity. The axis of symmetry for the latter is the Z-axis noted in the figure. Thus there is no azimuthal (about Z) dependence and the patterns shown completely describe the radiation. The patterns for the spherical cavity show the small deviation from spherical symmetry that was previously pointed out.

Radiation patterns are shown in Figure 8 for the two alternate assumptions for the static behavior of the double-couple terms. In either case the P wave pattern does not deviate strongly from spherical symmetry until we reach fairly high frequencies. Further, at 1 and 3 Hz there is not much difference between the two solutions. However, at the frequencies important for far-field surface waves and M_s, 0.05 and 0.1 Hz, the S waves range from very large to very small, depending upon our assumptions about the static limit.

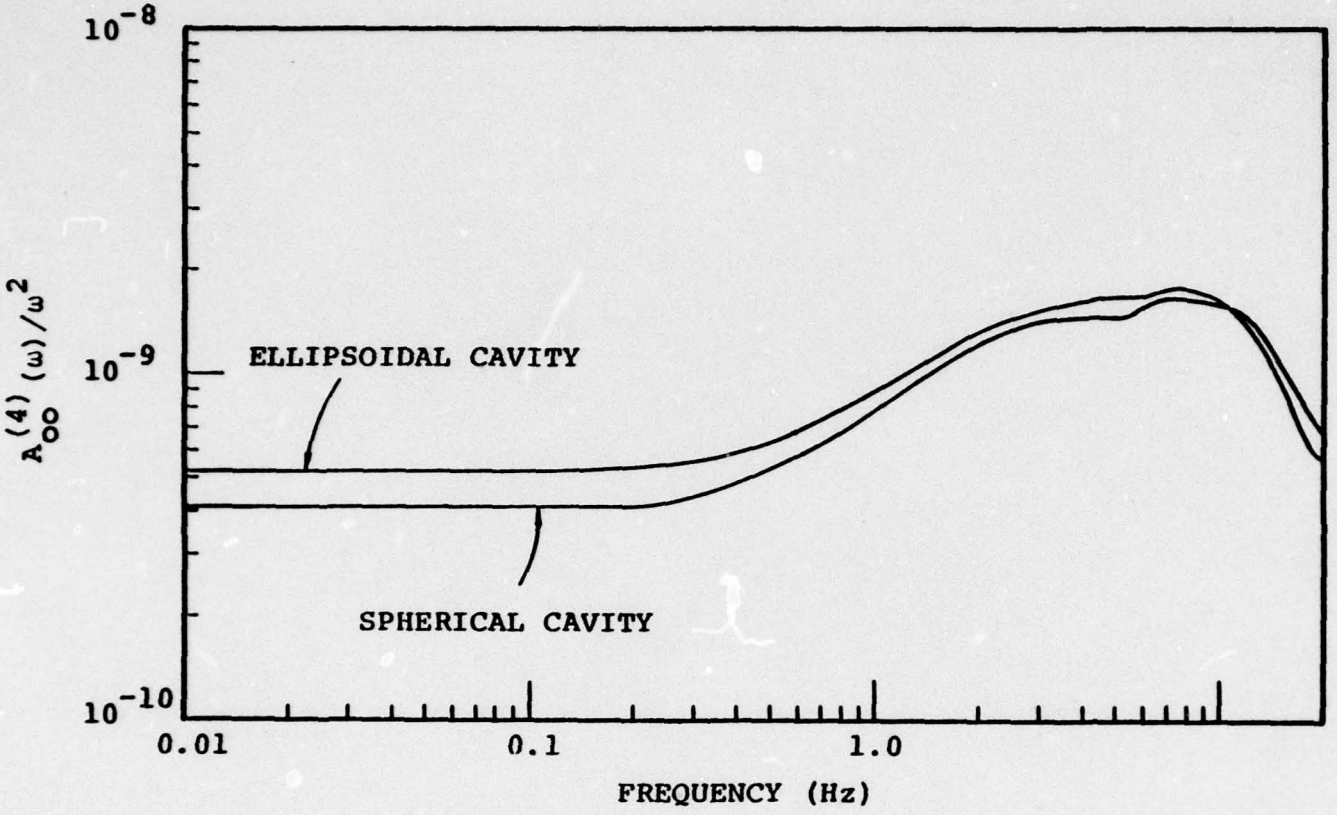

Figure 6. The normalized monopole terms are compared for the two source calculations.

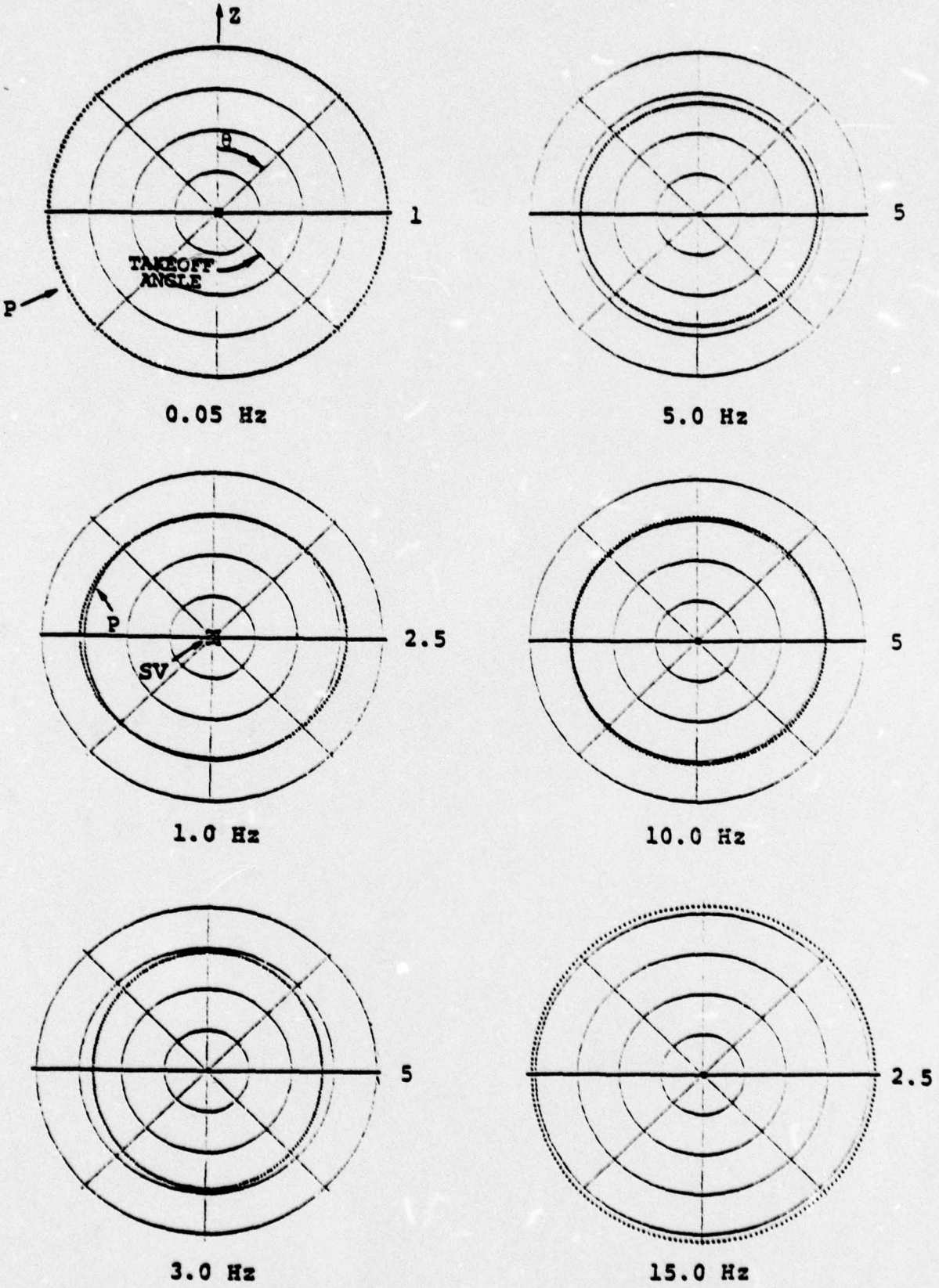

Figure 7. Radiation patterns are shown at six frequencies for the spherical cavity. The displacement amplitude for the innermost circle is shown at the right, normalized to that for the 0.05 Hz case.

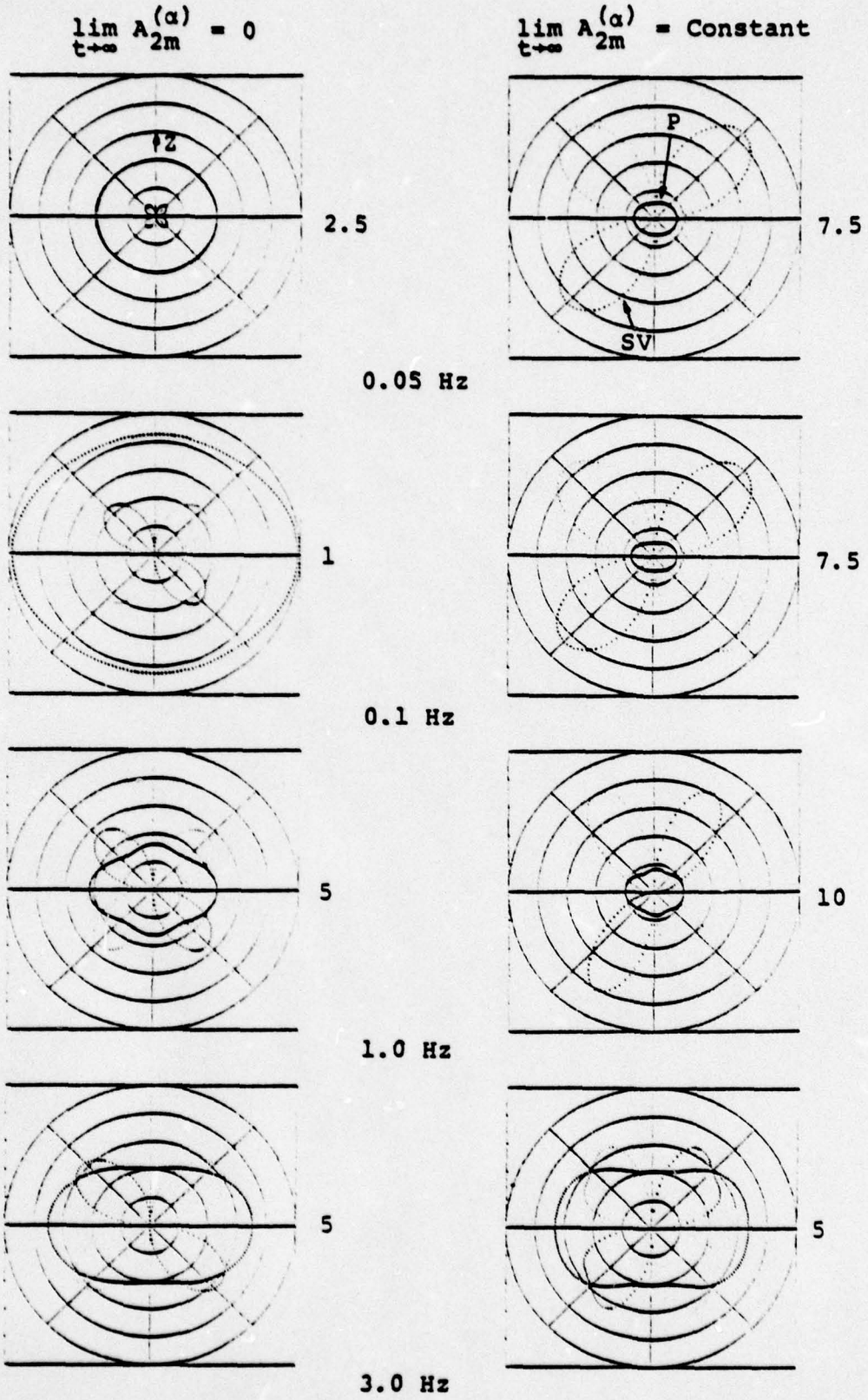

Figure 8. Radiation patterns are shown at seven frequencies for the ellipsoidal cavity. The patterns in the left column assume the double-couple vanishes at the late-time while those in the right column assume a finite static value. The amplitudes are normalized to the 0.05 Hz case in Figure 7.

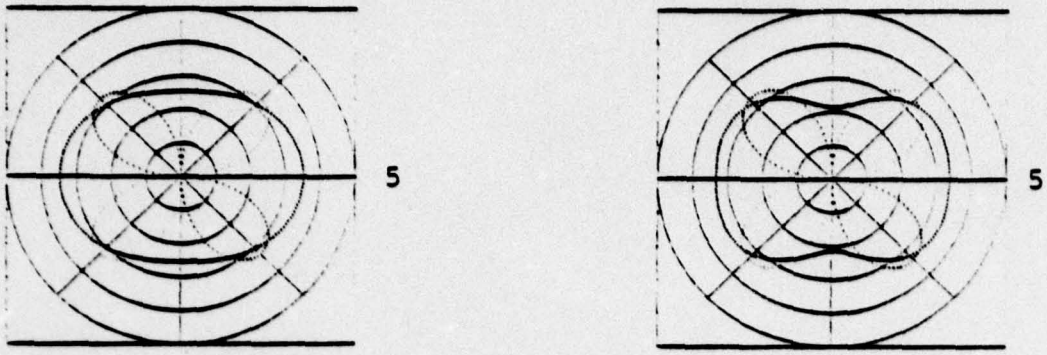

5.0 Hz

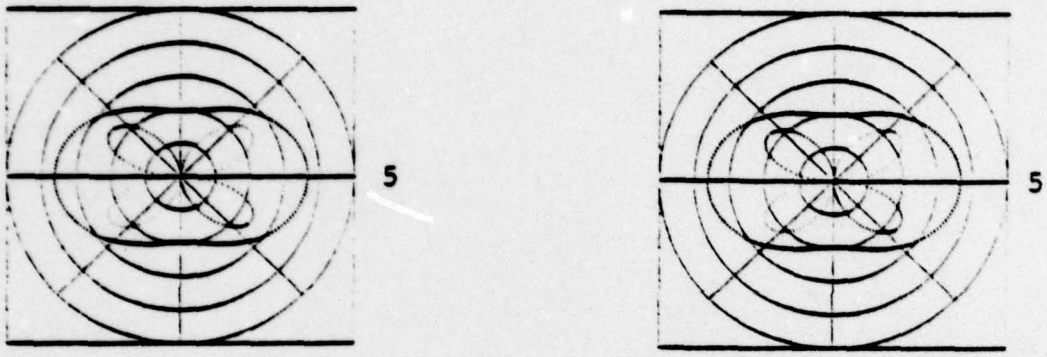

10.0 Hz

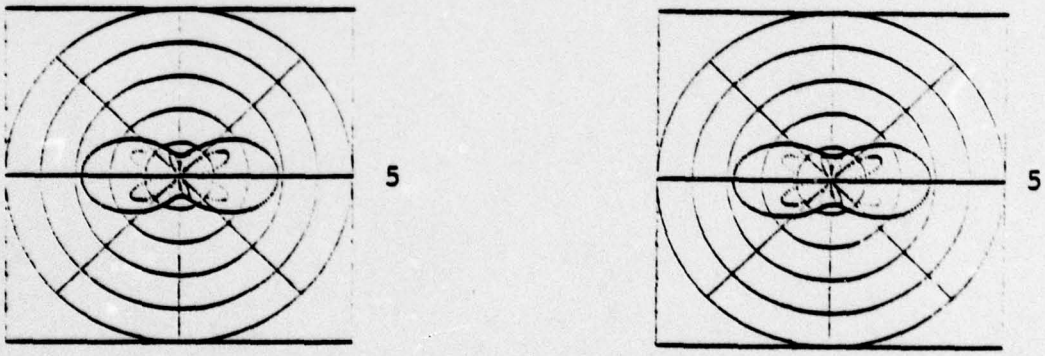

15.0 Hz

Figure 8. (continued)

The source for the spherical cavity can also be represented in terms of a reduced velocity potential using Equation (7) or (9). In Figure 9 we show the $|\hat{\Psi}|$ computed from the $\nabla \cdot \underset{\sim}{u}$ monitored at two stations located at $\theta = 10°$ and $\theta = 30°$. The differences between the two are expected in view of the fact that this source is not quite spherically symmetric.

Also plotted in Figure 9 is the $|\hat{\Psi}|$ computed from the monopole (Figure 6) using Equation (7). The potentials computed directly from the $\nabla \cdot \underset{\sim}{u}$ compared to that from the monopole differ by a significant amount at the long period end. Since the monopole represents a spatial average of the $\nabla \cdot \underset{\sim}{u}$; that is,

$$A_{oo}^{(4)}(R,t) = \int_o^{\pi/2} \nabla \cdot \underset{\sim}{u}(R,t) \sin\theta d\theta \quad , \tag{15}$$

from Equation (1), the estimate based on the monopole is probably more accurate.

As an estimate of the amount by which the explosions studied here are decoupled in Figure 10, we compare the monopole source function from Figure 9 to two estimates for the source function for coupled explosions. The Mueller/Murphy source function (Mueller and Murphy, 1971) is based on a fit to the SALMON data. Therefore, it can be taken to represent our empirical experience in this material. The S^3 source function 255 was computed with one-dimensional finite difference methods for a tamped explosion at a depth of 500 meters and is described by Bache, Cherry and Mason (1976). It represents computational results for explosions in this material.

The decoupling factors are indicated on Figure 10. The decoupling is largest at long periods and decreases rapidly with increasing frequency above one Hertz.

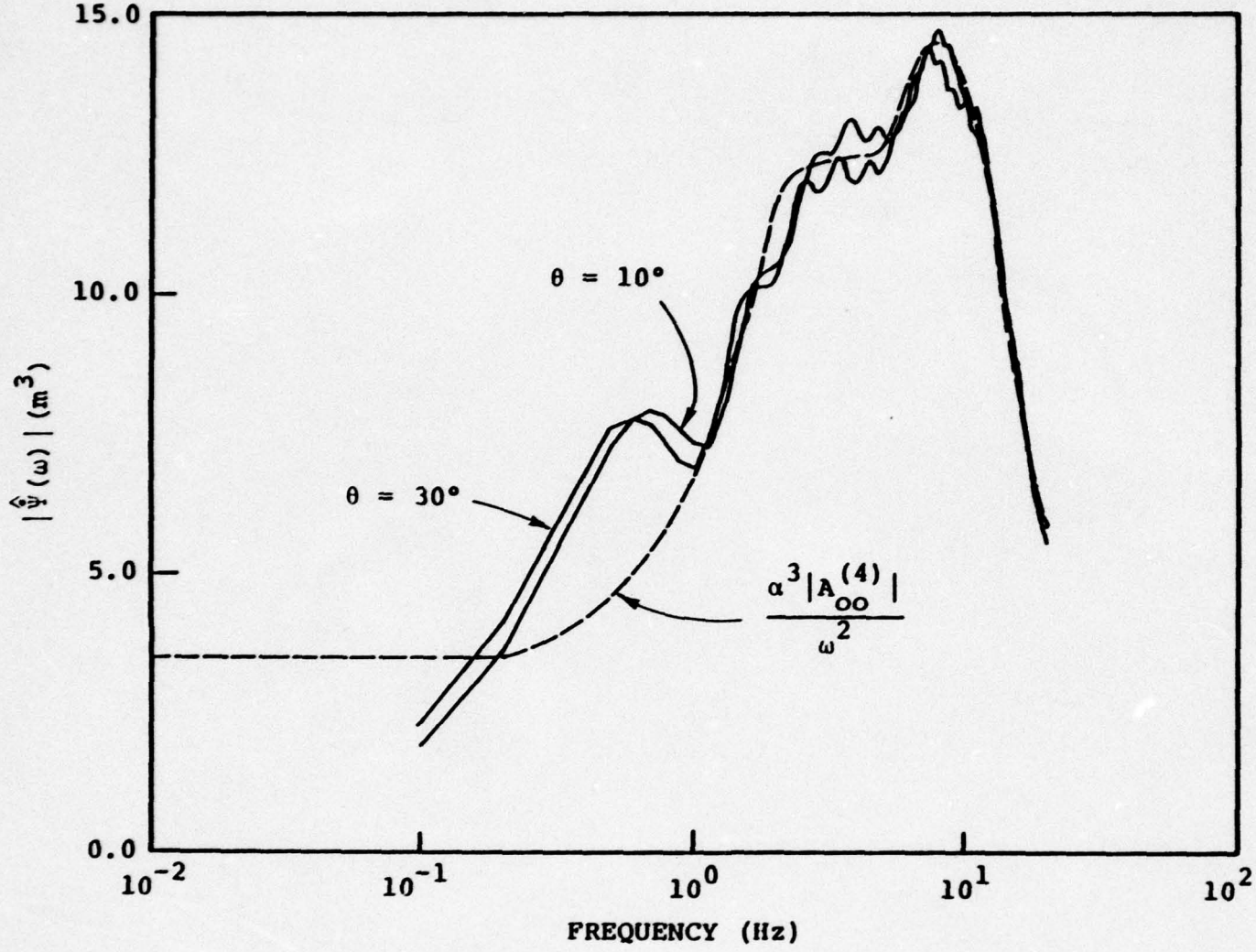

Figure 9. Three estimates of the reduced velocity potential for the spherical cavity calculations are compared.

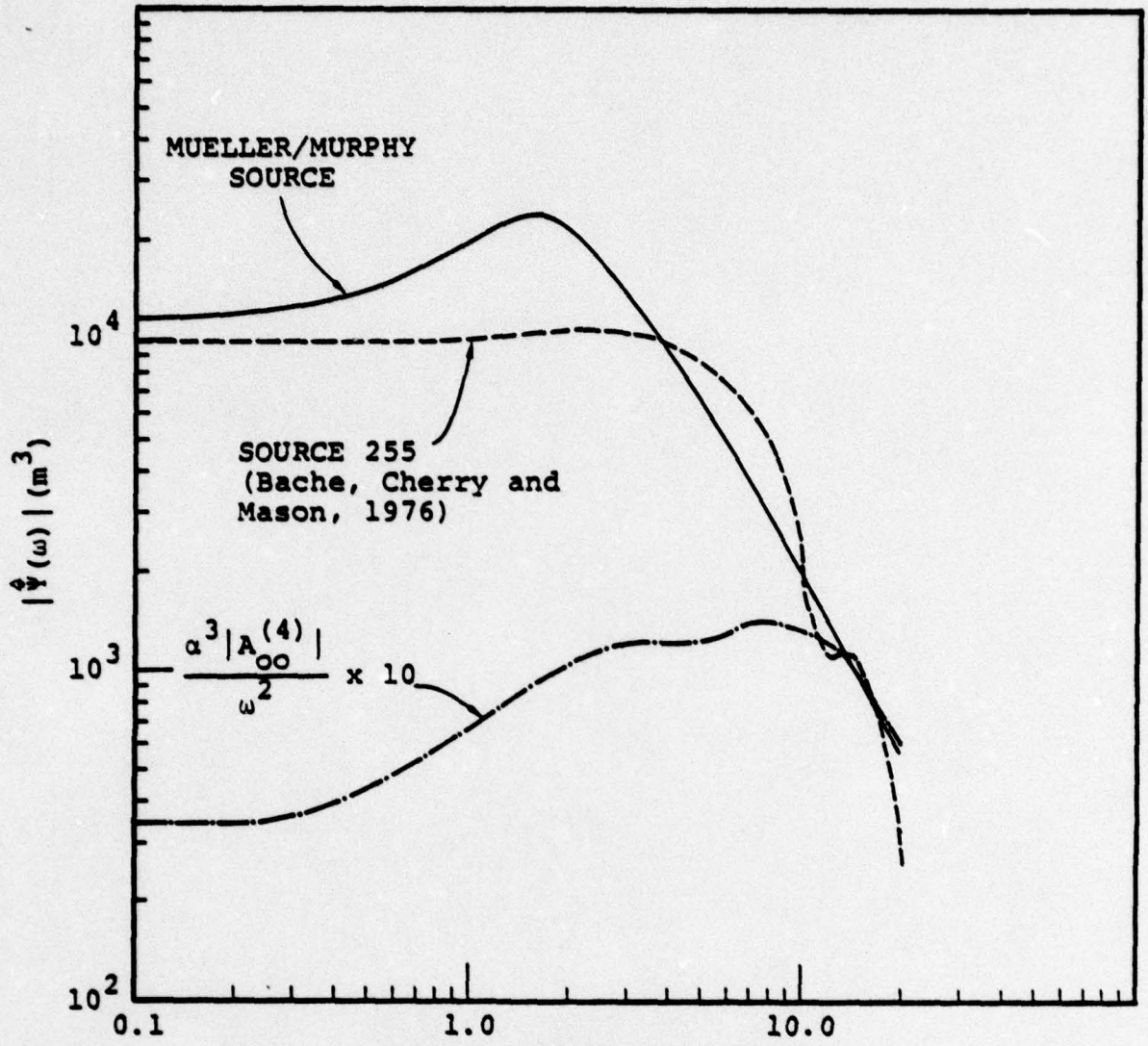

Decoupling Factors

Period	Mueller/Murphy Source	Source 255
0.1	325	282
0.5	310	220
1.0	298	151
3.0	114	86
5.0	52	67
10.0	14	16
20.0	9	6

Figure 10. The source function from Figure 9 is compared to two estimates for the source function for a fully coupled explosion in salt. The decoupling factor is computed with the Mueller/Murphy source.

6. BODY WAVE SEISMOGRAMS

Using the multipole coefficients presented in the previous section we can compute body and surface wave seismograms in the same way as done by Bache, Masso and Mason (1977). For the body waves we did the following:

- The source is embedded in the crustal structure tabulated in Table 2.
- The calculations are for a depth of 820 meters.
- The body waves were computed for a ray parameter of 0.079 sec/km. This corresponds to a distance of 36°. The takeoff angle for the source is then 20.4° from the vertical for the P and pP phases and 11.4° from the upward vertical for the sP phase. The delay times are P-pP = 0.45 seconds and P-sP = 0.71 seconds.
- The P waves were multiplied by 0.95×10^{-4} to represent the geometric spreading for a range of 36°, 1.77 to account for the free surface at the receiver and an operator for anelastic attenuation with $t^* = 0.7$.
- The response of a short period seismograph was also included.
- The m_b is then computed from

$$m_b = \log \frac{A}{T} + 3.32 \quad . \tag{16}$$

The synthetic seismograms are shown in Figure 11. From top to bottom, the sources are as follows:

1. The source 255 of Bache, Cherry and Mason (1977) is used.

TABLE 2

SOURCE REGION CRUSTAL STRUCTURE

Depth (km)	Thickness (km)	α (km/sec)	β (km/sec)	ρ (gm/cm^3)
0.12	0.12	2.1	0.75	1.7
0.37	0.25	3.3	1.64	1.8
3.0	2.63	4.4152	2.50	2.24
5.0	2.0	4.6	2.60	2.5
8.0	3.0	5.0	2.70	2.7
-	-	6.0	3.50	2.8

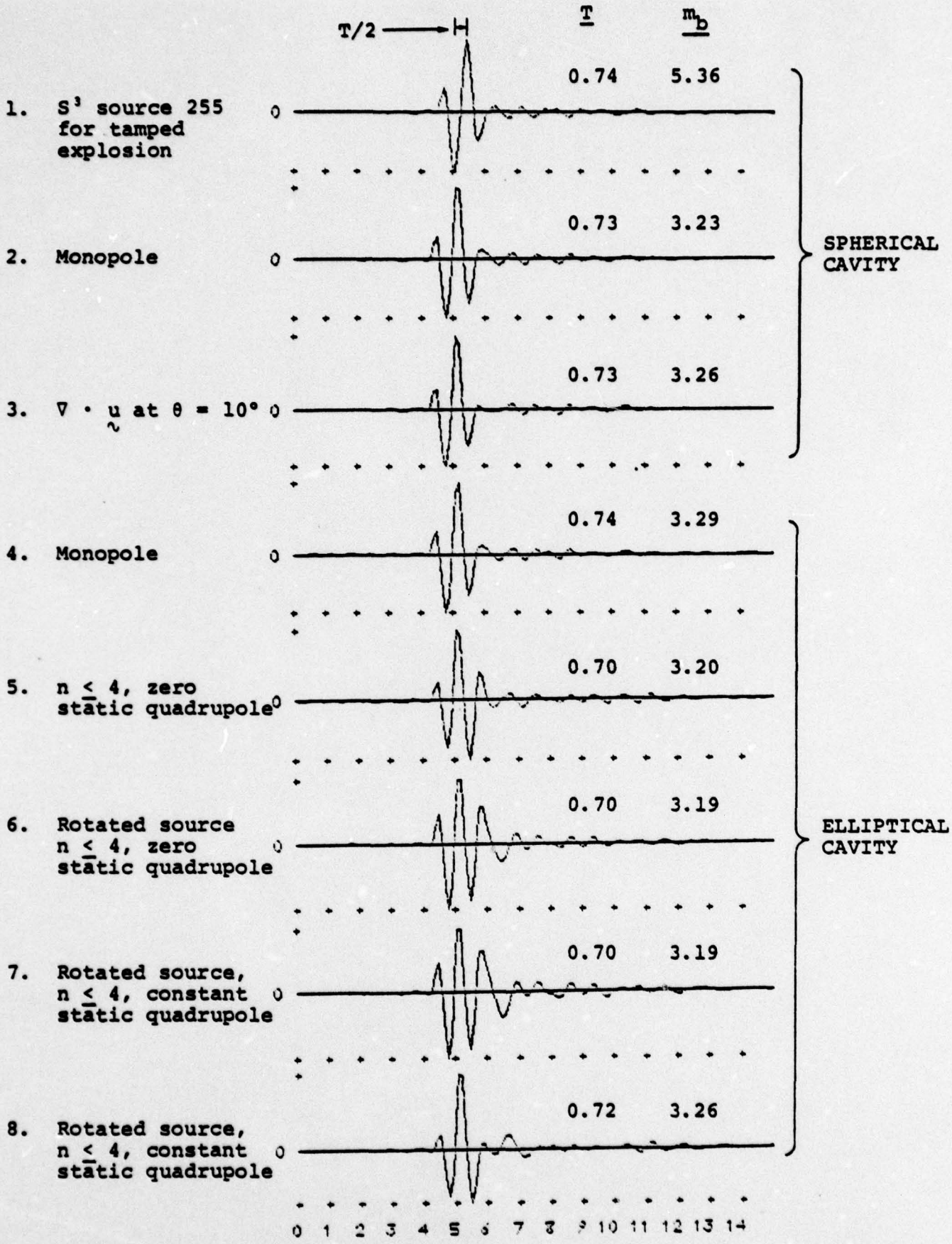

Figure 11. Synthetic seismograms are plotted for the eight sources described in the text. The m_b phase which has period T is the half-cycle indicated at the top.

2. The source is the monopole for the spherical cavity.

3. The source is the $\hat{\Psi}(\omega)$ computed from the $\nabla \cdot \underset{\sim}{u}$ for the spherical cavity at $\theta = 10°$.

The source functions for the first three seismograms were compared in Figures 9 and 10. The other seismograms are for the elliptical cavity for which the multipole coefficients were shown in Figure 5. These are:

4. The source is the monopole term of the expansion of the radiation field; that is, the spherically symmetric part.

5. Terms up to n = 4 are included with a zero static value assumed for the quadrupole. The 1 Hz radiation pattern for this source is shown on the left side of Figure 8.

6. The source is the same as for Item 5 but is rotated to maximize the contribution from the sP phase.

7. Terms up to n = 4 are included with a constant static value assumed for the quadrupole. The source is then rotated as for Item 6; that is, to maximize the sP phase. The 1 Hz radiation pattern for this source is shown in Figure 12. It should be compared to the patterns in Figure 8.

8. The source is the same as that shown in Figure 12 for Item 7 but has been rotated 54° counterclockwise to give an sP phase that is on the "-" lobe. That is, the sP phase for this case is the negative of that for Seismogram 7.

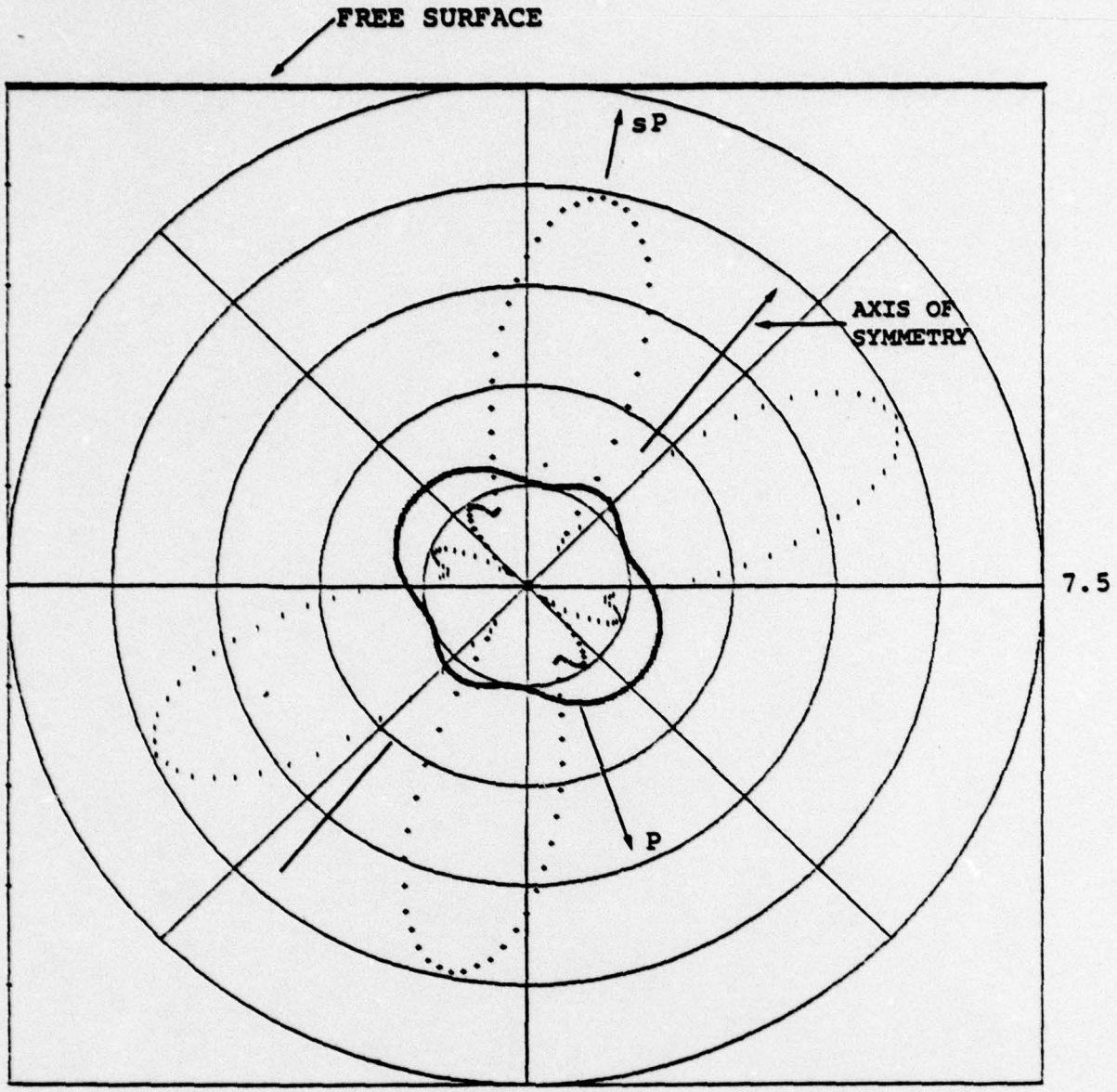

Figure 12. The radiation pattern is plotted for the source for seismogram 7 of Figure 11. The axis of symmetry has been rotated 38° from the vertical.

The seismograms for the eight sources are shown in Figure 11 together with the m_b data for each one. The results are consistent with our expectations from the analysis of the multipole coefficients and source radiation patterns. The important points are as follows:

- Our tamped source 255 leads to m_b values that are more than two units larger than for the decoupled sources.
- The three calculations for spherically symmetric sources, 2, 3, and 4, give about the same result. The spherically symmetric part of the field from the elliptical cavity is slightly larger than that from the spherical cavity.
- The assumption about the late-time behavior of the quadrupole has no importance for short period body waves.
- Changing interference between P, pP and sP as the source orientation is varied leads to some minor variations in m_b and the waveforms. This interference also depends on source depth, as is also the case for spherically symmetric explosions.

We conclude that radiation pattern effects are unimportant for the short period body waveforms and m_b.

7. SURFACE WAVE SEISMOGRAMS

The surface wave calculations are essentially the same as in Bache, Rodi and Harkrider (1978) and Bache, Masso and Mason (1977). The path model is the North American crustal

model of McEvilly (1964). In the source region this is modified by replacing the top three kilometers with the top three kilometers of the model in Table 2. The Q operator is that of Tryggvason (1965). An LRSM long period seismometer response is used. The seismograms were computed at 3000 km. The M_s was computed using the Marshall and Basham (1972) formula which is

$$M_s = \log A + 1.08 + P(T) \tag{17}$$

where A is the maximum peak-to-peak amplitude near 20 seconds and P(T) is a period correction tabulated by Marshall and Basham (1972). The P(T) is 0.05 at 24 seconds and zero at 20 seconds.

The surface wave amplitudes will be proportional to the long period level of the source functions discussed in Section 5. The only aspect that is not entirely clear is the extent of the radiation pattern effects introduced by the higher order terms.

Surface wave seismograms are shown in Figure 13. The sources for these calculations are listed below. The first three are for spherically symmetric sources and the others are for the elliptical cavity.

1. S^3 calculated source 255 for a 25 kt tamped explosion in salt is used.

2. The source is the monopole for the spherical cavity.

3. The source is the $\hat{\Psi}(\omega)$ computed from the $\nabla \cdot \underset{\sim}{u}$ at $\theta = 10°$ for the spherical cavity.

4. The source is the monopole, the spherically symmetric term, in the expansion of the radiation field for the elliptical cavity.

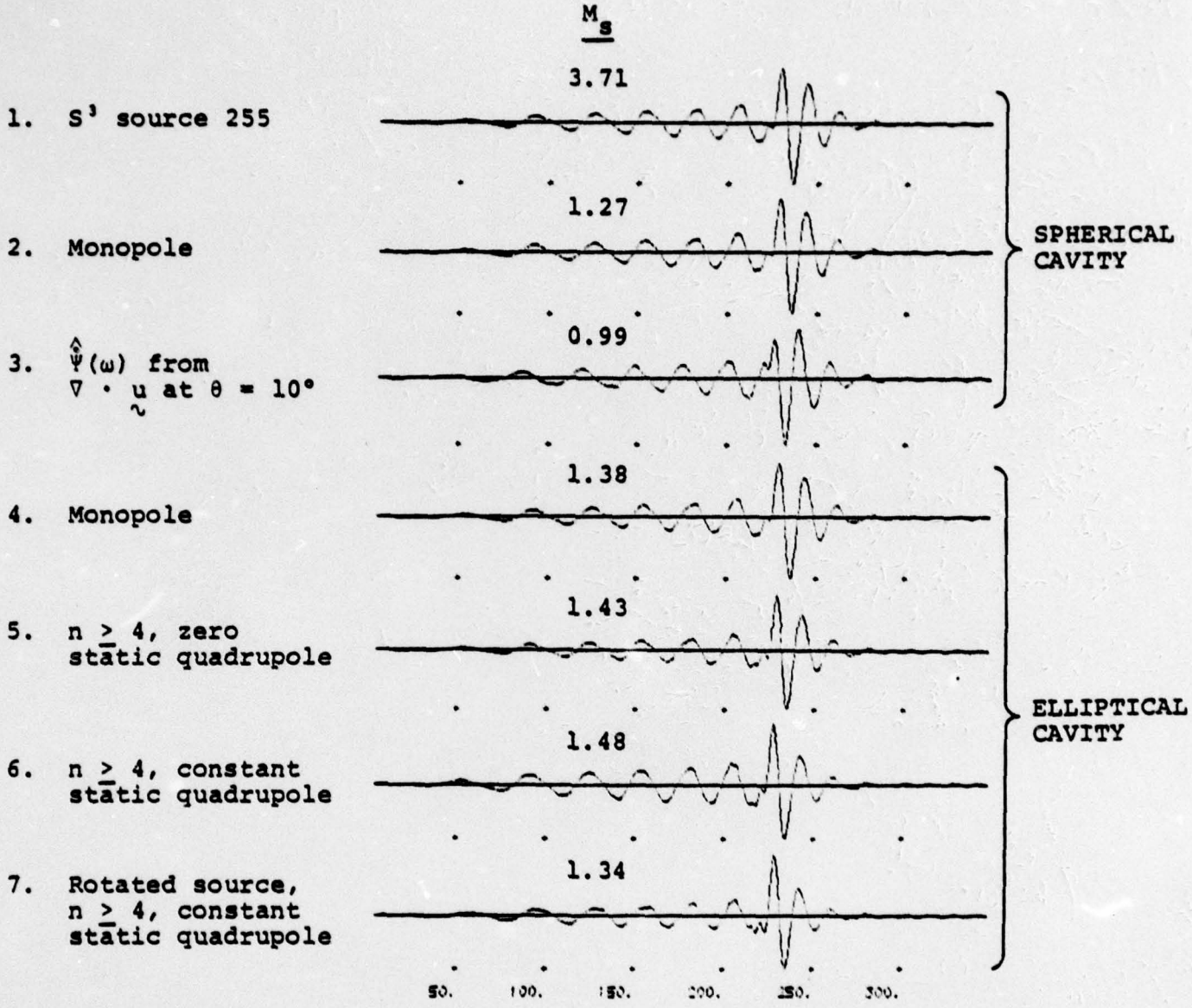

Figure 13. Theoretic seismograms are compared for seven sources.

5. Terms up to n = 4 are included with a zero static value assumed for the quadrupole. The source orientation is vertical.

6. Terms up to n = 4 are included with a constant static value assumed for the quadrupole. The source orientation is vertical.

7. The source is the same as in Item 6 but has been rotated to the orientation shown in Figure 12.

The M_s values are indicated on the seismograms of Figure 13. They are entirely consistent with the spectral amplitudes and radiation patterns shown in Section 5. For the spherical sources the M_s values are as expected from Figures 9 and 10. The source 255 gives an M_s that is 2.4 to 2.7 units larger than for the decoupled explosion in the spherical cavity. The multipole coefficient source, the monopole, is 0.28 M_s units larger than that estimated from a single $\nabla \cdot \underset{\sim}{u}$ time history. Also, the spherically symmetric part of the source for the elliptical cavity is somewhat bigger, about 0.11 M_s units, then that for the spherical cavity.

The M_s values for the seismograms of Figure 13 and a number of others are summarized in Table 4. Also shown in the table are the spectral amplitudes at 20 seconds. For the elliptical cavity both the M_s and the logarithm of the 20 second spectral amplitudes are normalized to the value for the monopole term taken alone. These values demonstrate clearly that the addition of higher order terms to the source representation has only a small effect.

TABLE 4

SUMMARY OF SURFACE WAVE AMPLITUDE DATA

Source	Azimuth	M_s	20 Second Spectral Amplitude	Normalized M_s	Normalized Spectrum
Spherical Cavity					
S^3 Source 255	-	3.71	11.9	-	-
Monopole	-	1.27	0.042	-	-
$\dot{\Psi}(\omega)$ from $\nabla \cdot \underset{\sim}{u}$ at $\theta = 10°$	-	0.99	0.023	-	-
Elliptical Cavity					
Monopole	-	1.38	0.054	0	0
$n < 4$, zero static value for quadrupole	-	1.43	0.058	0.05	0.03
$n < 4$, constant static value for quadrupole	-	1.48	0.061	0.10	0.05
Rotated Source, $n < 4$, constant static value for quadrupole	0	1.46	0.060	0.08	0.04
	45	1.47	0.060	0.09	0.04
	60	1.46	0.059	0.08	0.04
	90	1.45	0.058	0.07	0.03
	135	1.47	0.060	0.09	0.04
	- 15	1.41	0.058	0.03	0.03
	- 30	1.39	0.056	0.01	0.01
	- 45	1.37	0.054	-0.01	-0.01
	- 90	1.34	0.050	-0.04	-0.04
	-135	1.37	0.054	-0.01	-0.01

8. COMPARISON TO RESULTS FROM SIMILAR CALCULATIONS

Several years ago S[3] studied the teleseismic field from explosions in cylindrical cavities. The results were reported by Cherry, Bache and Patch (1975). The explosions were tamped, so the decoupling issues raised here were not considered. However, the radiation field did include a large S wave component with the same character as that for the elliptical cavity studied here. Therefore, it is useful to compare results of the two studies. We should also mention a unique aspect of the work described by Cherry, Bache and Patch. That is, some small-scale experiments were done to help verify the computational results.

Two calculations were done. In the first calculation a step pressure was introduced into a two-to-one aspect ratio cylindrical cavity as shown in Figure 14. The material response was restricted to the linear elastic regime. The resulting far-field radiation pattern is shown at several source orientations in Figure 15. This pattern applies for all frequencies below about 3 Hz. Comparing to Figure 8, we see it is about the same as the pattern at f = 0.1 Hz for the zero static quadrupole case.

The second calculation studied by Cherry, Bache and Patch was a full-scale simulation of a 27 kt nuclear explosion in a 3 meter diameter, 200 meter long tunnel in saturated tuff. The calculation was done by linking an Eulerian hydrodynamic program with a Lagrangian wave propagation program. Two far-field radiation patterns for this source are shown in Figure 16. At long periods the P wave field is significantly perturbed but the S wave excitation is small.

In the previous report we concluded that the short period waveforms and m_b were essentially the same as from a spherical tamped explosion. However, we reported a substantial effect on the Rayleigh wave amplitude and M_s. This conclusion was based

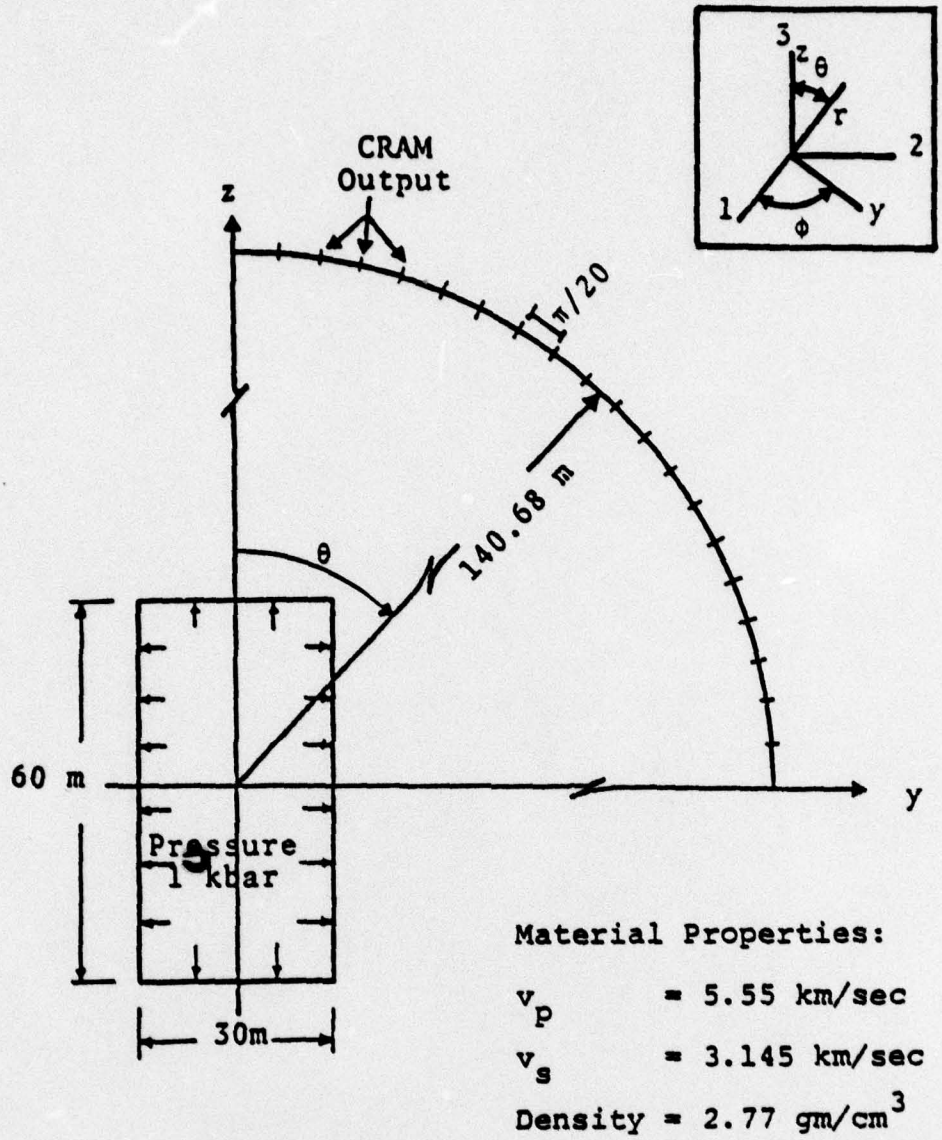

Figure 14. The coordinate system, geometry and physical parameters characterizing the linear elastic source calculation. The inset shows the relation between the cartesian (1,2,3), CRAM (y,z) and spherical (r,θ,φ) coordinate systems.

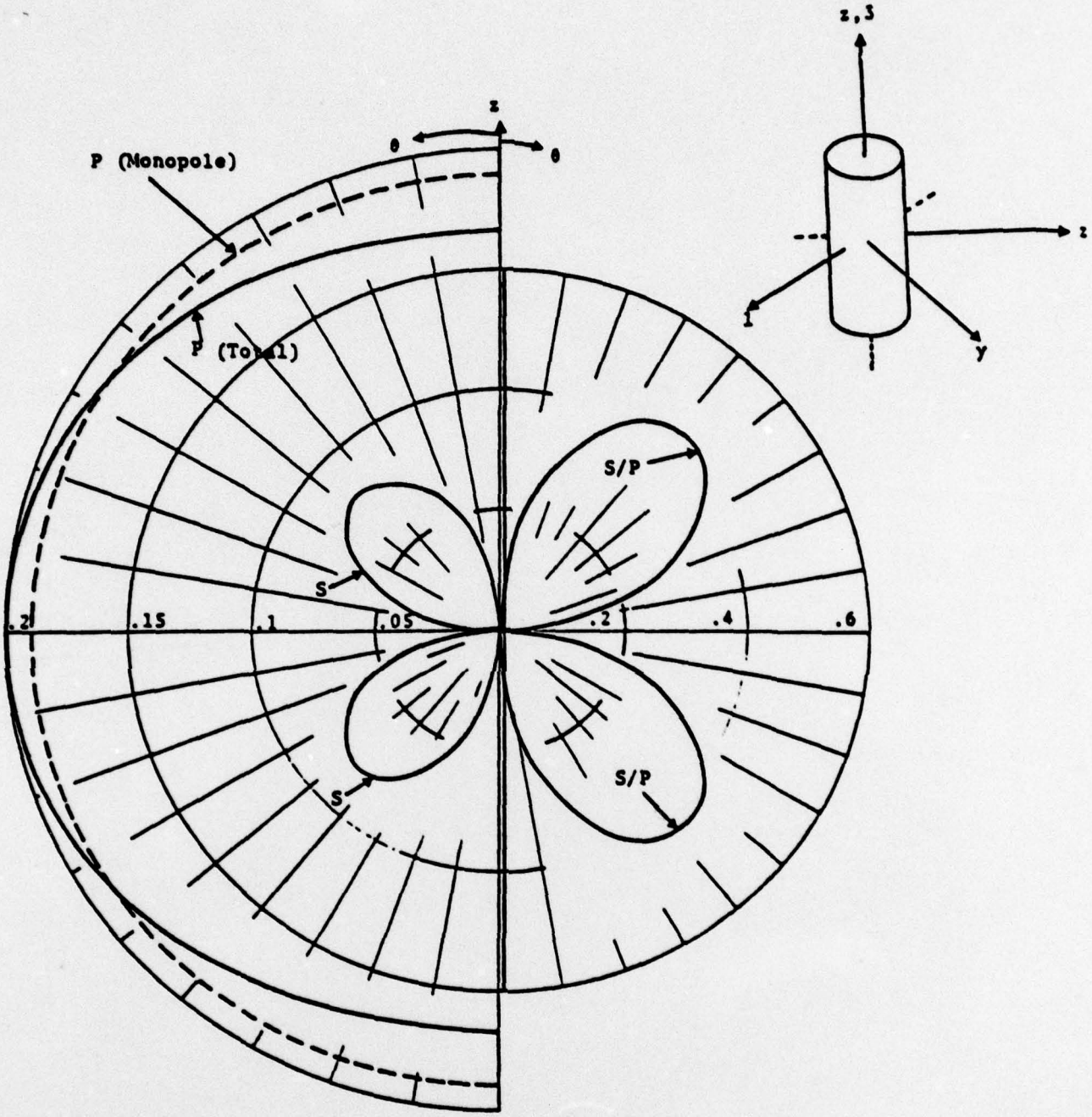

Figure 15. The far-field displacement radiation pattern (f < 3 Hz) 10 km from the source of Figure 14. The P wave radiation from the monopole alone is also indicated, as is the ratio of S to P wave displacements (on the right half of the figure) for the total source.

on calculations that were later discovered to be in error. In this report we will give the correct results.

The Rayleigh wave excitation was studied at three source orientations, vertical, horizontal and at 45°. The M_s values were calculated in the usual way. The "M_s enhancement" was then defined as the difference between the M_s from the total source and from the monopole term taken alone. For the source oriented vertically (as in Figures 15 and 16) the M_s enhancement is 0.09 for the linear elastic source and -0.10 for the 27 kt explosion in tuff.

The M_s enhancement was calculated at a number of azimuths to define the radiation pattern for the source oriented horizontally and at 45° from the vertical. These patterns are plotted in Figures 17 and 18. The difference between the largest and smallest M_s enhancement is shown as well as the average over the pattern. It is clear that the effect is quite small. We must conclude that this kind of source asymmetry has only a weak potential effect on the Rayleigh wave amplitudes.

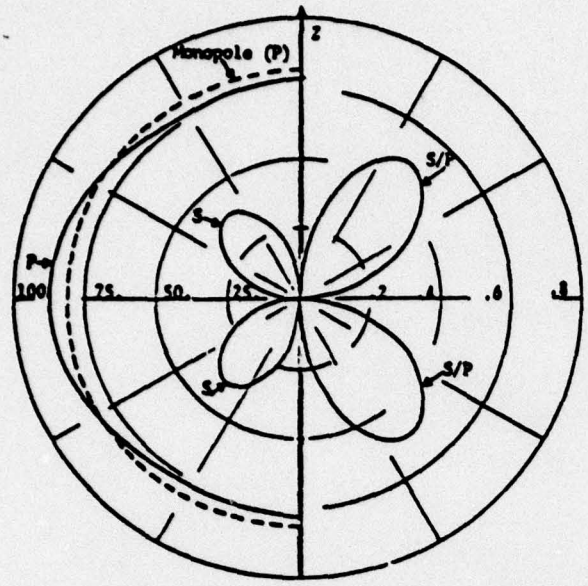

(a) One second radiation pattern.

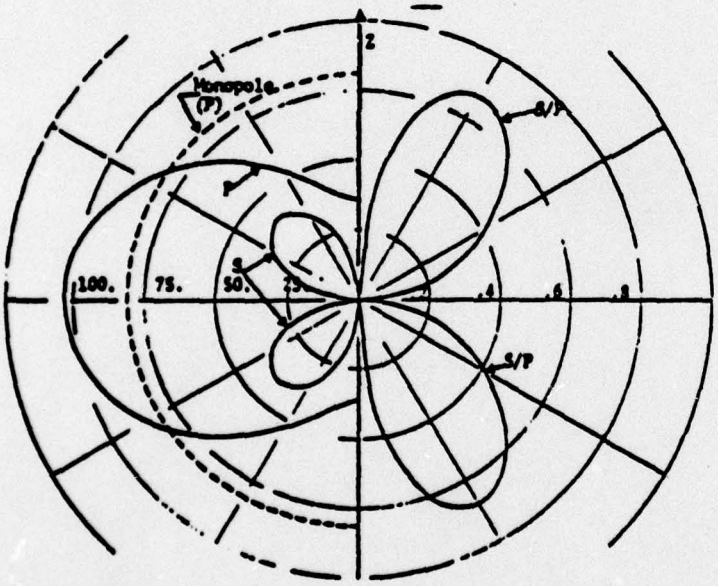

(b) Twenty second radiation pattern.

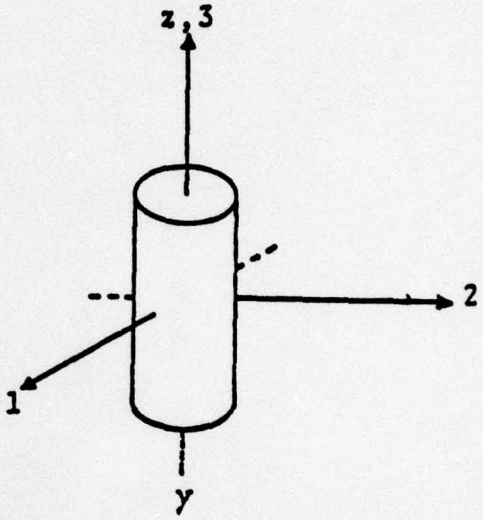

Figure 16. Far-field displacement radiation pattern 10 km from the nonlinear source of Section 7. Both 1 and 20 second patterns are shown and the ratio of S to P wave displacements are indicated on the right half of each pattern. The P wave radiation from the monopole alone is also indicated.

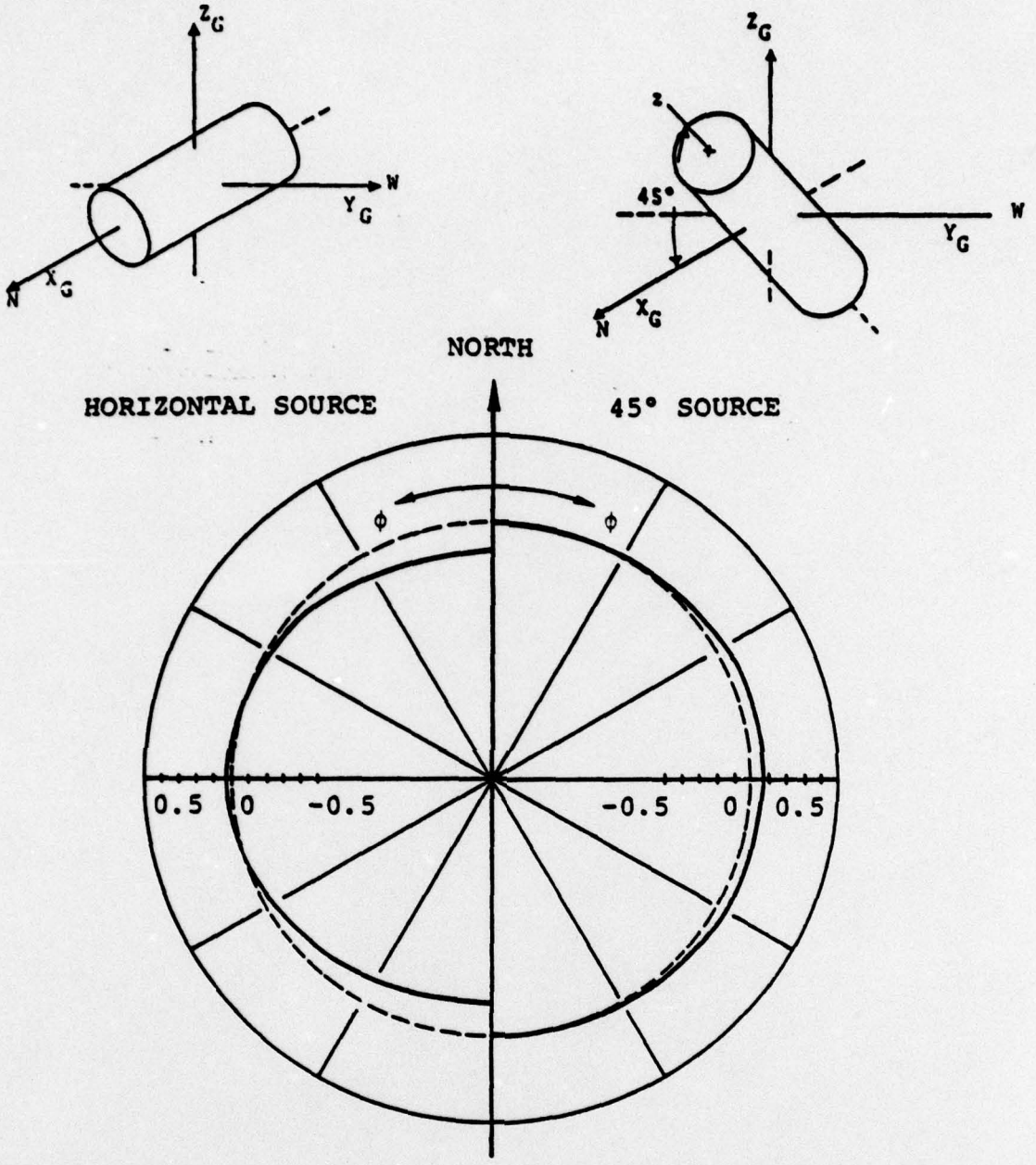

AVERAGE M_s ENHANCEMENT: -0.08
LARGEST M_s-SMALLEST M_s = 0.21

AVERAGE M_s ENHANCEMENT: 0.03
LARGEST M_s-SMALLEST M_s = 0.08

Figure 17. The azimuthal distribution of M_s enhancement is plotted for the linear elastic source oriented horizontally (left) and at 45° (right).

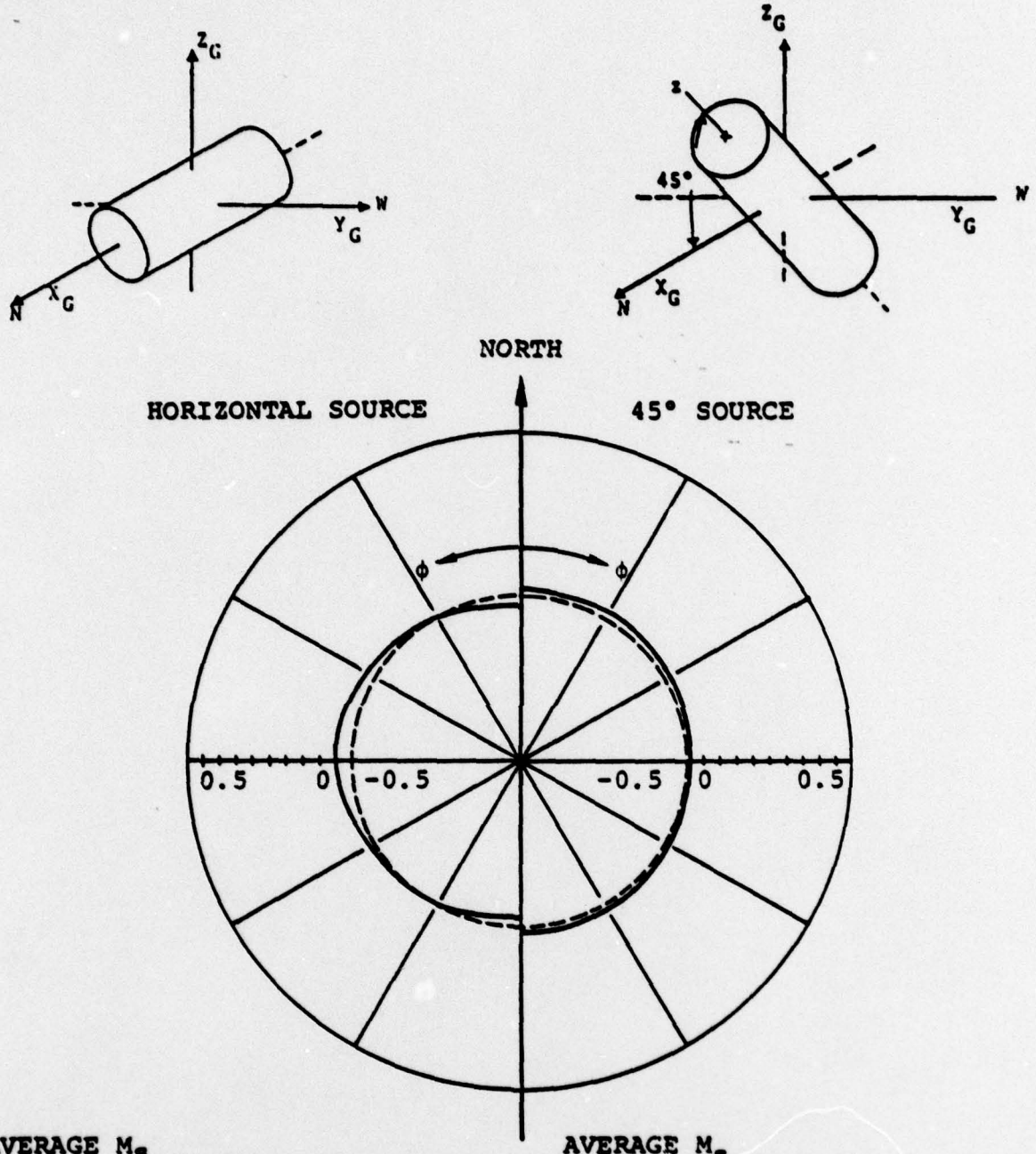

Figure 18. The azimuthal distribution of M_s enhancement is plotted for the 27 kt explosion calculation oriented horizontally (left) and at 45° (right).

REFERENCES

Bache, T. C. and D. G. Harkrider (1976), "The Body Waves Due to a General Seismic Source in a Layered Earth Model: 1. Formulation of the Theory," BSSA, 66, p. 1805-1819.

Bache, T. C., J. T. Cherry and B. F. Mason (1976), "The Dependence of Body Wave Magnitude on Yield for Underground Explosions in Salt," Systems, Science and Software Topical Report submitted to ARPA/VSC, SSS-R-77-3057, November 1976.

Bache, T. C., J. F. Masso and B. F. Mason (1977), "Theoretical Body and Surface Wave Magnitudes for Twelve Numerically Simulated Cratering Explosions," Systems, Science and Software Topical Report submitted to ARPA/VSC, SSS-R-77-3119, January 1977.

Bache, T. C., W. L. Rodi and D. G. Harkrider (1978), "The Crustal Structures Inferred from Rayleigh Wave Signatures of NTS Explosions," submitted to BSSA.

Cherry, J. T., T. C. Bache and D. F. Patch (1975), "The Teleseismic Ground Motion Generated by a Nuclear Explosion in a Tunnel and Its Effect on the M_s/m_b Discriminant," Systems, Science and Software Final Contract Report to the Defense Nuclear Agency, DNA 3645F, May 1975.

Harkrider, D. G. and C. B. Archambeau (1978), "Theoretical Rayleigh and Love Waves from an Explosion in a Prestressed Source Region," to be submitted for publication.

Marshall, P. D. and P. W. Basham (1972), "Discrimination Between Earthquakes and Underground Explosions Employing an Improved M_s Scale," Geophys. J., 28, p. 431-458.

McEvilly, T. V. (1964), "Central U. S. Crust-Upper Mantle Structure from Love and Rayleigh Wave Velocity Inversion," BSSA, 54, pp. 1997-2016.

Minster, J. B. (1977), "Transformation of Multipolar Source Fields Under a Change of Reference Frame," Geophys. J., 47, pp. 397-409.

Tryggvason, E. (1965), "Dissipation of Rayleigh Wave Energy," JGR, 70, pp. 1449-1455.